The Astronomical Journal, 171:29 (22pp), 2026 January https://doi.org/10.3847/1538-3881/ae1b8a

52 Eclipsing Quadruple Star Candidates Discovered in TESS Full Frame Images

V. B. Kostov[1,2], B. P. Powell[1], S. A. Rappaport[3], T. Borkovits[4,5,6], R. Gagliano[7], M. Omohundro[8], T. L. Jacobs[9], M. H. Kristiansen[10], G. Torres[11], G. Handler[12], A. R. Schmitt[13], H. M. Schwengeler[14], T. Mitnyan[4,5,15], I. A. Terentev[16], D. M. LaCourse[17], A. Vanderburg[11], S. D. Alexandrov[18,19], C. M. da Silva[18], Marco Z. Di Fraia[18], Aline U. Fornear[18], M. Huten[18], D. Iannone[18], Julien S. de Lambilly[18], S. Lee[18], J. Orosz[20], R. Rodrigues[18], A. Tarr[18], and W. Welsh[20]

[1] NASA Goddard Space Flight Center, 8800 Greenbelt Road, Greenbelt, MD 20771, USA; veselin.b.kostov@nasa.gov
[2] SETI Institute, 189 Bernardo Avenue, Suite 200, Mountain View, CA 94043, USA
[3] Department of Physics, Kavli Institute for Astrophysics and Space Research, MIT, Cambridge, MA 02139, USA
[4] Baja Astronomical Observatory of University of Szeged, H-6500 Baja, Szegedi út, Kt. 766, Hungary
[5] HUN-REN—SZTE Stellar Astrophysics Research Group, H-6500 Baja, Szegedi út, Kt. 766, Hungary
[6] Konkoly Observatory, Research Centre for Astronomy and Earth Sciences, H-1121 Budapest, Konkoly Thege Miklós út 15-17, Hungary
[7] Amateur Astronomer, Glendale, AZ 85308, USA
[8] Citizen Scientist, c/o Zooniverse, Department of Physics, University of Oxford, Denys Wilkinson Building, Keble Road, Oxford, OX13RH, UK
[9] Amateur Astronomer, Missouri City, TX, USA
[10] Brorfelde Observatory, Observator Gyldenkernes Vej 7, DK-4340 Tølløse, Denmark
[11] Center for Astrophysics | Harvard & Smithsonian, 60 Garden Street, Cambridge, MA 02138, USA
[12] Nicolaus Copernicus Astronomical Center, Polish Academy of Sciences, ul. Bartycka 18, 00-716, Warszawa, Poland
[13] Citizen Scientist, 616 West 53rd Street, Apartment 101, Minneapolis, MN 55419, USA
[14] Citizen Scientist, Planet Hunter, Bottmingen, Switzerland
[15] Department of Experimental Physics, University of Szeged, H-6720, Szeged, Dóm tér 9, Hungary
[16] Citizen Scientist, Planet Hunter, Petrozavodsk, Russia
[17] Amateur Astronomer, 7507 52nd Place NE, Marysville, WA 98270, USA
[18] Citizen Scientist, Eclipsing Binary Patrol Collaboration, USA
[19] Institute of Plant Physiology and Genetics, Bulgarian Academy of Sciences, Acad. G. Bontchev Str., BI.23, Sofia 113, Bulgaria
[20] Department of Astronomy, San Diego State University, 5500 Campanile Drive, San Diego, CA 92182, USA
Received 2025 October 1; revised 2025 October 30; accepted 2025 October 30; published 2025 December 11

Abstract

We present the discovery of 52 eclipsing quadruple star candidates detected in TESS Full Frame Image ELEANOR data by machine learning and citizen scientists. The uniformly vetted and validated targets exhibit two sets of eclipses following two distinct periods, representing quadruple systems with a 2+2 hierarchical configuration. Detailed photocenter measurements confirmed that both sets of eclipses originate within ∼0.1–0.2 pixels (∼2″–4″) of the corresponding target, and ruled out resolved nearby field stars. The catalog includes a number of systems producing prominent eclipse timing variations and/or apsidal motion, a quadruple with an outer period of ∼1400 days, and even a 2+2 quadruple in a likely wide quintuple with a resolved comoving star. Additionally, two systems have complete astrometric solutions for the outer orbits from Gaia. We provide the measured ephemerides, eclipse depths and durations, and overall statistical properties, and we highlight potentially interesting systems that merit further investigations.

Unified Astronomy Thesaurus concepts: Eclipsing binary stars (444); Multiple stars (1081)

Materials only available in the online version of record: machine-readable table

1. Introduction

Multiple stellar systems are a fascinating natural outcome of stellar formation and evolution. Overall, more than half of Sun-like stars are in binary and higher-order hierarchical systems, and the higher the mass of the system, the higher the multiplicity fraction (e.g., D. Raghavan et al. 2010; M. Moe & R. Di Stefano 2017; A. Tokovinin 2018). Systems where one or more of the individual components happen to have the fortuitous geometrical orientation to produce eclipses present excellent targets for validation and confirmation of the underlying multiplicity, as well as ideal laboratories for testing and benchmarking stellar evolution models (e.g., J. Andersen 1991; G. Torres et al. 2010; O. Pejcha et al. 2013; J. A. Orosz 2015; X. Fang et al. 2018; G. Fragione & B. Kocsis 2019; B. Liu & D. Lai 2019; A. S. Hamers et al. 2021; C. S. Kochanek 2021; M. M. Shara et al. 2021; A. A. Trani et al. 2022; P. Vynatheya & A. S. Hamers 2022; V. B. Kostov et al. 2023; J. Kolář et al. 2025; P. Zasche et al. 2025). Of these, perhaps the most intriguing targets are those where the outer periods are short enough that the dynamical interaction between the components are not only detectable but allow *direct confirmation* of the systems' architectures (e.g., T. Borkovits et al. 2016, 2022a, 2022b; S. Rappaport et al. 2017; B. P. Powell et al. 2021a; V. B. Kostov et al. 2021b; T. Borkovits 2022; S. A. Rappaport et al. 2022, 2023). Speaking of dynamical interactions, these systems are invaluable testbeds for investigations of long-term orbital stability and secular evolution, including Von Zeipel–Lidov–Kozai cycles (e.g., H. von Zeipel 1910; Y. Kozai 1962; M. L. Lidov 1962; A. S. Hamers & D. Lai 2017). The physical and orbital properties of such systems offer important new insights into how they form (e.g., initial disk fragmentation, later

capture, or a combination) and evolve (e.g., similar to isolated single stars, or through complex multiple common envelope phases), and even constrain the presence of potential planets (e.g., R. D. Mathieu 1994; A. P. Whitworth 2001; J. E. Pineda et al. 2015; J. J. Tobin et al. 2016; V. B. Kostov et al. 2016, 2021b; A. Tokovinin 2021; H. P. Preece et al. 2022; J. Stegmann et al. 2022; T. Fragos et al. 2023).

From an observational perspective, compact 2+2 quadruple systems present unique challenges and opportunities. For example, the smaller the outer orbit is, the more direct imaging or astrometric observations would struggle to resolve it (e.g., A. Tokovinin 2018, 2021; S. Majewski et al. 2025). Another difficulty is that spectral lines from four unresolved stars can lead to significant blending, making it difficult to measure individual radial velocities (I. Czekala et al. 2017; T. Pribulla et al. 2020; B. P. Powell et al. 2025). With that said, when successful, such analyses can provide a wealth of information about the stellar properties, including effective temperatures, surface gravities, and elemental abundances for all four components. When both binary components of these systems produce eclipses, the composite lightcurve can exhibit complex patterns where overlapping (blended) eclipses create intricate photometric signatures that can be difficult to disentangle. This complexity often requires sophisticated modeling techniques and long-term monitoring to accurately determine the system parameters (e.g., V. B. Kostov et al. 2021a; T. Borkovits 2022; V. B. Kostov et al. 2023; B. P. Powell et al. 2025). However, it also presents an opportunity: the extremely rich information content in these lightcurves can provide precise measurements of stellar masses, radii, and orbital parameters for all four stars simultaneously.

All-sky photometric surveys provide excellent discovery platforms for such systems, and indeed the number of known eclipsing 2+2 quadruple candidates has dramatically increased in the past several years alone. Thanks to observations from ASAS-SN, Kepler, OGLE, TESS, and ZTF, hundreds of such candidates have already been detected (e.g., A. Prša et al. 2011, 2022; I. Soszyński et al. 2016; C. S. Kochanek et al. 2017; M. Deleuil et al. 2018; A. N. Heinze et al. 2018; ; T. Hajdu et al. 2022; N. Mowlavi et al. 2023; V. B. Kostov et al. 2022, 2024; D. M. Rowan et al. 2022; T. Vaessen & J. van Roestel 2024), dramatically expanding their family portrait and, in essence, transitioning the field from "cherry picking" to "cherry harvesting." It is important to note that these candidates have undergone various levels of vetting and validation, and most are yet to be confirmed as genuine quadruple systems. Such confirmation requires substantial efforts, typically based on extensive follow-up observations and analysis. These can include long-term photometric and spectroscopic monitoring to obtain new eclipse times and measure the radial velocities of the two component EBs, utilizing archival data, direct imaging to resolve the individual components, and comprehensive photodynamical modeling (e.g., V. B. Kostov et al. 2021b, 2023; T. Pribulla et al. 2023; B. P. Powell et al. 2025).

Here we present the latest addition of 52 targets to our TESS/GSFC/VSG (TGV) catalog of eclipsing stellar multiples with a $2+2$ hierarchical configuration. This brings the total number of TGV quadruples to 250, and represents a meticulously curated set of uniformly vetted, validated, and characterized systems where the two binary components are confirmed to originate from within ∼0.1–0.2 TESS pixels (∼2″–4″) of the target. In turn, this potentially makes the systems compact enough to detect dynamical interactions on observable timescales. For each system, we measure the ephemerides of both EBs, the respective eclipse depths and durations (including those of the secondary eclipses, if present), outline interesting systems and potential issues, include Gaia astrometric information, and provide relevant comments.

This paper is organized as follows. In Section 2 we highlight the detection, vetting, and validation of the quadruple candidates. Section 3 presents the details of the catalog and we summarize our results in Section 4.

2. Detection, Validation, and Vetting

All targets presented here produce two sets of eclipses following two distinct periods and are assumed to be unresolved at the time of writing.[21] An example is shown in Figure 1 for TIC 64832327 where the two component EBs produced prominent primary eclipses (and no discernible secondary eclipses). The analysis of the systems presented here followed the methodology of V. B. Kostov et al. (2022, 2024, K22, and K24 hereafter). For completeness, we outline the various steps below.

2.1. Detection

For the detection of the systems presented here, we relied on an established collaborative effort between advanced computational techniques and expert human visual inspection. The underlying process leverages the natural synergy between state-of-the-art machine learning algorithms and trained citizen scientists, enabling efficient exploration of the vast datasets generated by TESS. Briefly, this is a two-step process that generally goes as follows.

First, we identified the target stars as EB candidates through the application of a trained neural network to TESS Full Frame Image ELEANOR data for all stars brighter than $T = 15$ mag (B. P. Powell et al. 2021a, 2022). Notably, the network was trained to detect lightcurves exhibiting one or more eclipse-like features—rather than a strict sequence of consecutive eclipses—focusing solely on morphological characteristics without imposing periodicity requirements (V. B. Kostov et al. 2025). This process effectively reduced the number of unique targets necessitating subsequent manual review by 2 orders of magnitude, i.e., from millions of lightcurves per sector to tens of thousands.

Most of the targets discussed in this catalog were identified by members of the Visual Survey Group (VSG; M. H. K. Kristiansen et al. 2022), comprising highly skilled volunteers conducting visual inspections of preselected lightcurves. These experts employ specialized software tools, including LcTools and custom-designed programs (A. R. Schmitt et al. 2019; A. Schmitt & A. Vanderburg 2021), to perform on-demand and in-depth analysis of the photometric data. Their extensive experience enables rapid and accurate identification of salient features, with typical assessment times on the order of seconds per lightcurve (K22, K24). The remaining targets were identified through the

[21] Targets where Gaia DR3 measurements (Gaia Collaboration et al. 2021) suggest that one EB may be comoving with a resolved nearby EB—thus potentially indicating a (very) wide quadruple system—are beyond the scope of this work and excluded from our TGV catalog.

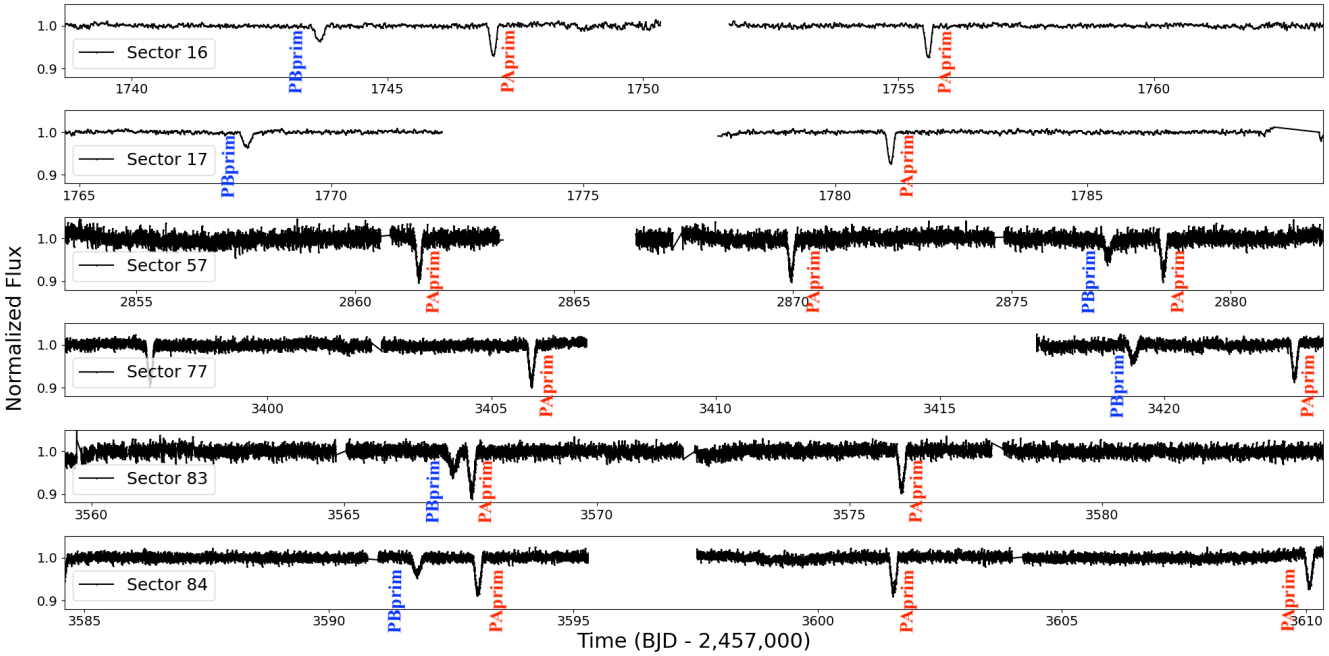

Figure 1. An illustrative example of an eclipsing quadruple candidate detected in TESS FFI ELEANOR data. The panels show six sectors of data for TIC 64832327, exhibiting two sets of primary eclipses with two distinct periods, labeled as PAprim (13 red events) and PBprim (6 blue events).

Table 1
Example False Positives Mimicking Two Sets of On-target Eclipses in TESS Lightcurves

TIC	False Positive
2768366	CO
2775663	CO
2844449	CO
4254645	FSCP
5049897	CO
5092088	CO
5109750	CO
8698910	FSCP
10072325	CO
11469030	CO
11793277	CO

Note. "CO" refers to "centroid offset," i.e., photocenter measurements show that one EB (or both) is off-target; "FSCP" refers to "field star in central pixel," i.e., there is a resolved field star that is bright enough to produce one EB (or both) as contamination, but is too close to the target star ($\lesssim$0.1–0.2 pixels) for the photocenter measurements to pinpoint the origin of the eclipses.

(This table is available in its entirety in machine-readable form in the online article.)

Eclipsing Binary Patrol project (EBP; V. B. Kostov et al. 2025), a Zooniverse-hosted citizen science initiative aimed at vetting and validation of the EB candidates detected by the neural network of V. B. Kostov et al. (2025).[22] As part of the EBP workflow, the volunteers inspect the presented lightcurve and have the option to flag interesting features such as additional eclipses.

It is worth noting that the contributions of volunteer astronomers to professional astronomical research are substantial, resulting in numerous peer-reviewed publications and significant discoveries of a large number of transiting planets and multiple star systems (e.g., M. H. K. Kristiansen et al. 2022, and references therein). As an example, members of the VSG have visually inspected millions of lightcurves from Kepler, K2, and TESS, and have identified numerous unique objects such as triply eclipsing triples, quadruple star systems, tidally tilted pulsators, and exocomets, underscoring the critical importance of citizen science (e.g., G. Handler et al. 2020; B. P. Powell et al. 2021b; B. K. Capistrant et al. 2022; M. H. K. Kristiansen et al. 2022; T. Pribulla et al. 2023; R. Jayaraman et al. 2024; G. Handler et al. 2025). To ensure their analysis is as thorough as possible, the volunteers also examine publicly available archives and databases such as Simbad, Gaia, ZTF, etc., as well as alternative TESS data processing pipelines such as QLP (C. X. Huang et al. 2020) and SPOC (J. M. Jenkins et al. 2016) for select targets. This multifaceted approach maximizes the fidelity of the potential candidates and increases the probability of them being genuine quadruple systems.

2.2. Validation and Vetting

Given the relatively large pixel size of TESS (21″), it comes as no surprise that the vast majority of candidates for stellar multiples detected by the citizen scientists turn out to be false positives due to the presence of distinct, spatially resolved eclipsing binaries in close proximity to the target star. Indeed, TESS lightcurves are frequently affected by such occurrences, as well as various other astrophysical sources of contamination (variable stars, solar system objects, etc.), and nonastrophysical artifacts (e.g., L. Cacciapuoti et al. 2022; C. Magliano et al. 2023; V. B. Kostov et al. 2025). Notably, the issue of contamination is neither unique to TESS, nor uncommon. Instead, it presents a general challenge across different photometric surveys and datasets, and requires careful scrutiny. As an example, P. Zasche (2024) report that about one in four of the eclipsing quadruple candidates (R. Z. Ádám

[22] https://www.zooniverse.org/projects/vbkostov/eclipsing-binary-patrol

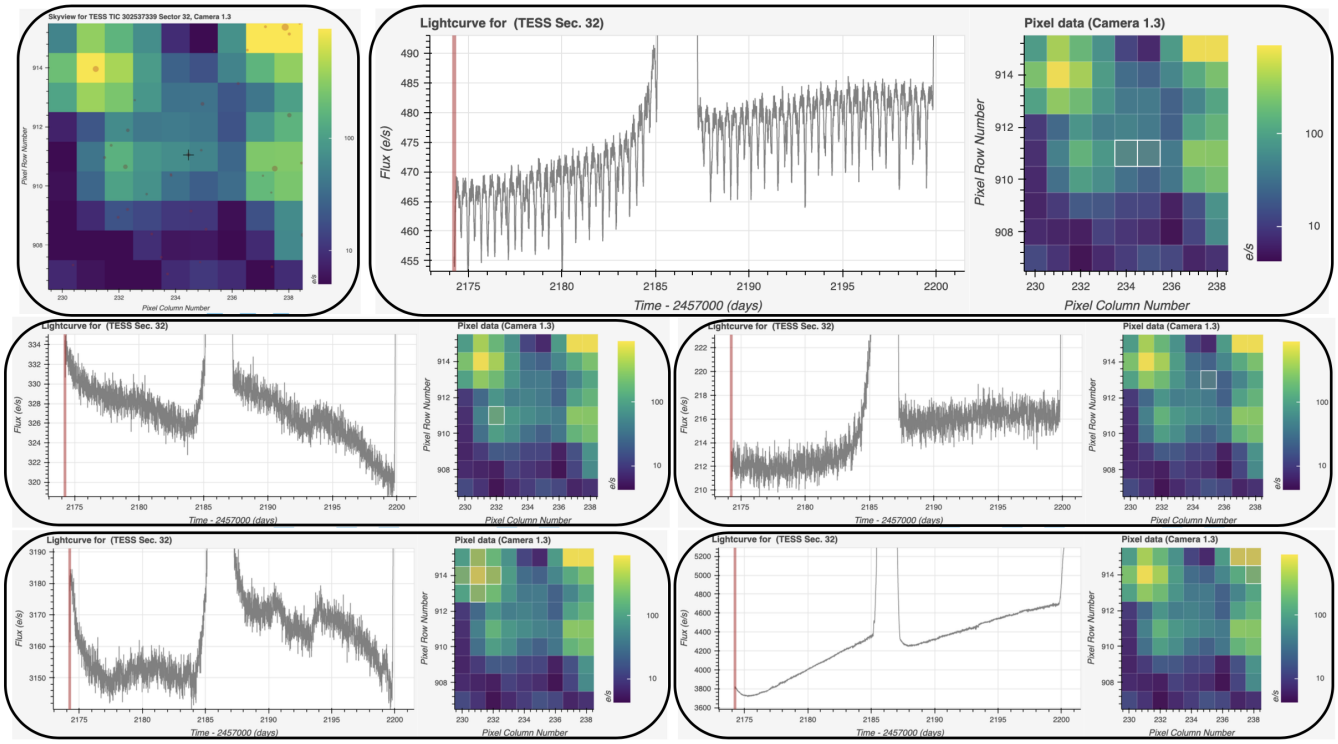

Figure 2. Pixel-by-pixel analysis of the quadruple candidate TIC 302537339 for Sector 32. First row, left panel: 9 × 9 TESS pixels difference image centered on the target. There are several nearby field stars bright enough to contaminate the target's lightcurve and mimic a quadruple candidate. First row, right two panels: lightcurve (left) from the two pixels centered on the target (right, white contours). Second and third rows: same as above but for the nearby field stars. None of these show features resembling the eclipses seen in the target's lightcurve, confirming the signals originate from the vicinity of TIC 302537339. For clarity, the individual panels are outlined with black contours.

et al. 2023) detected in OGLE data are in fact false positives due to unrelated nearby EBs.

Consequently, each of the quadruple candidates identified by the citizen scientists must undergo a series of rigorous vetting and validation procedures. Below we elaborate on our multitiered methodology for addressing the contamination challenge, presenting examples, discussing known limitations and relevant considerations. For more details, we refer the reader to K22, K24, and V. B. Kostov et al. (2025).

In order of decreasing angular separation between the target and nearby contaminating stars, our three "lines of defense" in validating potential quadruple candidates are as follows:

1. *Pixel-by-pixel analysis*. This is a common procedure based on manual inspection of the TESS image. Specifically, we employ Lightkurve's interactive features (Lightkurve Collaboration et al. 2018) by first locating the target star's pixel position and selecting an appropriate aperture to minimize contamination from resolved sources. Next, we examine the adjacent pixels individually for the presence of nearby unrelated EBs that may mimic a second set of eclipses detected in the target's lightcurve. Finally, we rule out adjacent pixels and verify that both sets of eclipses originate from the vicinity of the target. An example of this vetting is shown in Figure 2 for the case of TIC 302537339. Candidates passing this initial inspection proceed to the next level of scrutiny—a more detailed photocenter vetting.
2. *Photocenter analysis*. Another commonly used vetting method employs a difference imaging technique to analyze the center-of-light motion during detected features of interest such as transits or eclipses. This process involves creating difference images by subtracting the in-eclipse images (how TESS sees the surrounding pixels during an eclipse) from the out-of-eclipse images (how TESS sees the surrounding pixels before and after the same eclipse) for each detected eclipse and available sector. The center-of-light of these difference images represents the pixel position of the eclipse source. To measure the pixel position of said center of light, we fit each difference image with a point-spread function and the TESS pixel response function (PRF) and adopt the average of the two measurements. Finally, the average measured photocenter pixel position from all detected eclipses is compared to the catalog pixel position of the target (according to the TIC; K. G. Stassun et al. 2019). If the difference between the two positions is not statistically significant, the corresponding eclipses are considered to be on-target. An example of this is shown in Figure 3 for TIC 470730552. Alternatively, the eclipses are marked as off-target and the candidate is flagged as a false positive. Overall, based on our experience with TESS data, and depending on the particular target, the photocenter positions can often be reliably measured to within ∼0.1–0.2 pixels (corresponding to ∼2″–4″) of the target (e.g., V. B. Kostov et al. 2022, 2024, 2025).

We note that the difference images should ideally look like the left panel in Figure 3, i.e., a single, bright, well-defined pixelated "spot" centered near the target's position and superimposed on an otherwise dark

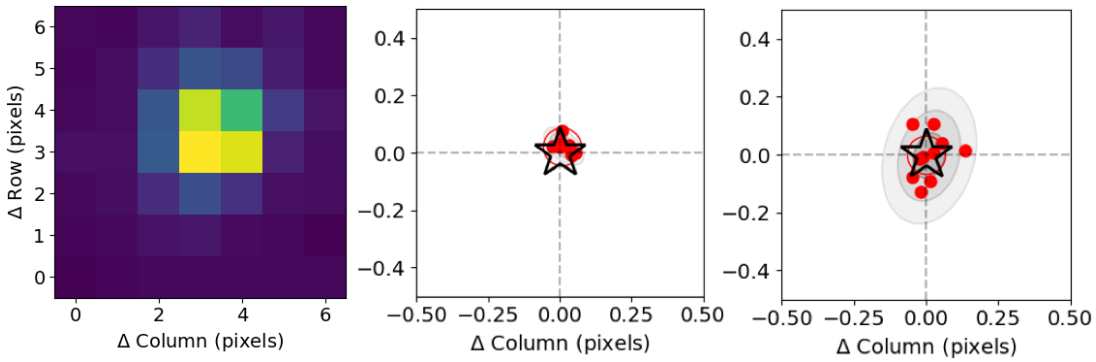

Figure 3. Left panel: 7 × 7 TESS pixel difference image centered on TIC 470730552 for Sector 58. Middle and right panels: measured photocenters for PA (middle) and PB (left panel). The small red dots, the large red circle, and the black star represent the per-eclipse photocenters, the average photocenter, and the pixel position of the target, respectively. Note that the scale of the left panel is 10 times larger than that of the middle and left panels.

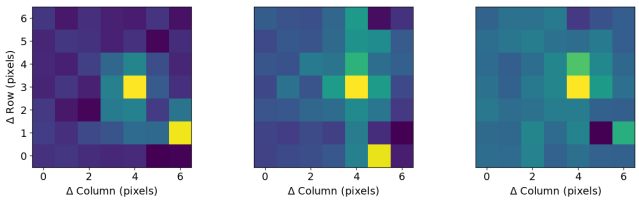

Figure 4. Same as left panel of Figure 3 but for three eclipses of TIC 2158899 from Sector 44. All three difference images are affected by systematics, making them less than ideal for photocenter measurements.

background. In practice, the difference images can often be affected by systematics that distort them, sometimes even to the point of making them unsuitable for photocenter measurements; these systematics are target-specific and generally vary from one eclipse to another. An example of this is shown in Figure 4 for three eclipses of TIC 2158899 in Sector 44. Thus, to minimize the impact of such distortions on the photocenter measurements and ensure their reliability, we visually inspect the difference image for each eclipse. Those that do not pass scrutiny are removed from the analysis.[23]

3. *Magnitude difference ($\Delta_{\rm mag}$) as a function of measured eclipse depth ($\delta_{\rm ecl}$).* Finally, there are instances where a resolved field EB is sufficiently bright to produce the detected "extra" eclipses as false positives, yet is too close to the target star to pinpointing their origin. This occurs when said EB is within a magnitude difference with respect to the target star:

$$\Delta_{\rm mag} = 2.5 \times log_{10}\left(\frac{1 - 2 \times \delta_{\rm ecl}}{2 \times \delta_{\rm ecl}}\right). \quad (1)$$

If the projected separation between the two is smaller than ∼0.1–0.2 pixels, the true source of the extra eclipses cannot be definitively determined based on TESS photocenter measurements, the candidate is marked as unclear and excluded from the catalog. An example of this is shown in Figure 5 for the case of TIC 8698910, producing two distinct sets of eclipses. However, there is a resolved star 1.″83 away, TIC 668542259, with $\Delta_{\rm mag} \approx 1.1$ which makes pinpointing the origin of the two sets of eclipses highly challenging.

Altogether, this comprehensive vetting process ensures the reliability and consistency of the TGV catalog, minimizing false positives and providing a robust dataset for further research and analysis.

2.3. Ephemeris Determination and Eclipse Characterization

For all but 3 of the 52 candidates, we derived initial estimates of the orbital periods and eclipse times for both sets of detected eclipses utilizing the Box-Least Squares (BLS) algorithm (G. Kovács et al. 2002), applied to all available TESS FFI data at the time of writing. As part of this process, we removed data outliers and eclipses dominated by systematics, normalized the lightcurve on a sector-by-sector basis, stitched all sectors together, and, if necessary, detrended the data utilizing a low-order Savitsky–Golay filter. For the remaining targets, TIC 97642729, 391461666, and 79908874, the second EB does not produce enough eclipses in the available data to uniquely determine the orbital period.

Following the preliminary BLS analysis, we improved the ephemeris measurements and measured eclipse depths and durations by implementing custom models that fit each individual eclipse with a trapezoid, Gaussian, a generalized hyperbolic secant (see Equation (2), K22), and a generalized Gaussian function (see Equation (1), K22). Based on our experience, the latter two provide comparable fits to the data, and both are significantly better than either the trapezoid or the Gaussian model. For simplicity, the measurements reported in this catalog are based on the generalized Gaussian fits.

We note that while this approach does not provide any information on the astrophysical effects responsible for eclipses, it nevertheless represents a fast and flexible framework that comes with three key advantages:

1. *Eclipse depths and duration.* Eclipses come in a wide variety of shapes, depending on the a priori unknown physical and orbital parameters of the system. The two generalized functions easily accommodate this variety by reliably modeling the eclipse shapes observed in our target sample. This is highlighted in Figure 6 for the two components of the quadruple candidate TIC 20938739, where the primary eclipses for one of the EBs have a pronounced V-shape with a relatively sharp minimum,

[23] Partially or fully blended eclipses also render the difference imaging technique inapplicable, and are thus removed from the photocenter measurements as well. This situation can arise in eclipsing quadruple systems with similar periods and ephemerides, unlike in transiting multiplanet systems.

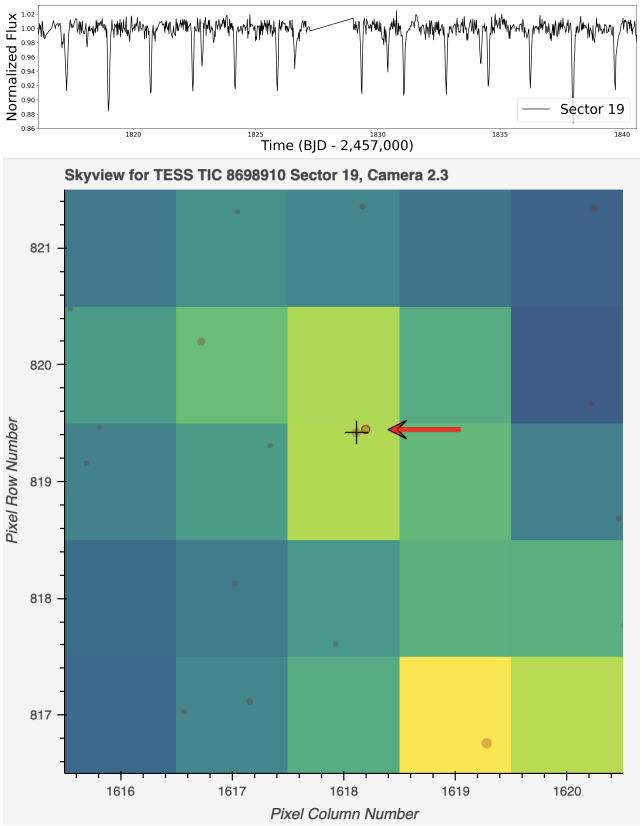

Figure 5. Upper panel: TESS FFI ELEANOR lightcurve for TIC 8698910 exhibiting two sets of eclipses. Lower panel: 5×5 pixel Skyview image centered on the target (black cross-hair symbol). There is a resolved field star separated by $1\farcs83$ and $\approx$1.1 TESS magnitude fainter (marked with a red arrow), making photocenter vetting of the detected eclipses difficult.

while those of the other have a much flatter bottom and resemble the letter U.

2. *Eclipse depth differences between different sectors.* Sometimes, eclipse depths appear to vary from one sector to another (see Figure 6). In the vast majority of cases, such depth variations are not astrophysical but instead caused by systematic effects that affect the lightcurve on a sector-by-sector basis. This is typically due to changes in the relative orientation and respective overlap between the sector-specific aperture used to extract the target's lightcurve and nearby field stars. Consequently, the effects of blending, contamination, and background subtraction can vary not only from one sector to another but also within a single sector, particularly across observation gaps caused by data downlink periods (e.g., M. N. Lund et al. 2021; R. Luque et al. 2023; G. Wang & N. Espinoza 2024; T. Han et al. 2025; V. B. Kostov et al. 2025). An example of one of the more extreme cases where systematics dominate the lightcurve is shown in Figure 7 for TIC 99629496, where the eclipses in Sector 80 are upside down. As above, both the generalized hyperbolic secant and the generalized Gaussian automatically circumvent this problem by providing independent depth measurements on an eclipse-by-eclipse basis. For simplicity, the eclipse depths reported in this catalog are the median values.
3. *Eclipse timing variations (ETVs).* Many EBs exhibit deviations from strict periodicity caused by dynamical

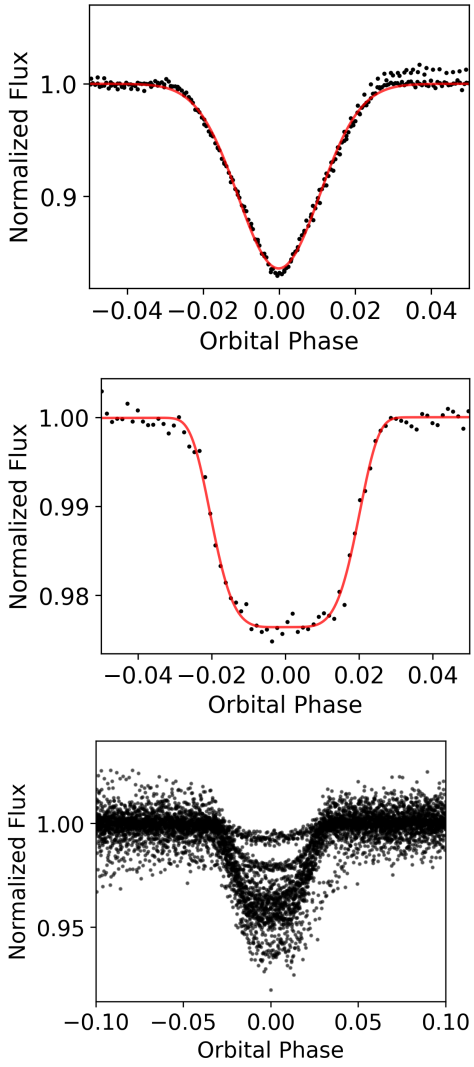

Figure 6. Upper and middle panels: generalized Gaussian model fits (red) for the primary eclipses of the PA $\approx$ 3.96 days component (upper) and PB $\approx$ 4.94 days (middle) component of the quadruple candidate TIC 20938739. The black dots represent the TESS FFI data for Sector 51. The two eclipses have notably different shapes—one being more *V*-shaped and the other more *U*-shaped—yet the model fits both. Lower panel: phase-folded primary eclipses of the PA $\approx$ 3.08 days component of the quadruple candidate TIC 97642729 showing TESS FFI data for all available sectors (6, 33, 43, 44, 45, 72, and 87). Due to systematic effects, the apparent eclipse depths vary dramatically between different sectors.

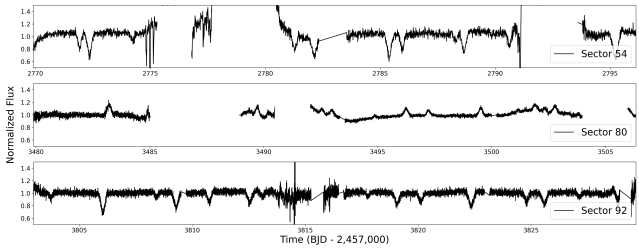

Figure 7. TIC 99629496: an example of systematics-dominated ELEANOR lightcurve where the eclipses are upside down in one sector of TESS data.

interactions with additional bodies in the system (e.g., J. A. Orosz 2015; T. Borkovits et al. 2016, 2025). Detecting such variations provides critical information about the underlying architecture of the system and can

Table 2
Parameters of the 52 Quadruple Candidates Presented Here, Including Ephemerides, Eclipse Depths and Durations, and Additional Comments

TIC ID	R.A.	Decl.	Bin	Period	$T_{0,p}$	$T_{0,s}$	ϕ_s	Dep_p	Dep_p(spr)	Dep_s	Dep_s(spr)	Dur_p	Dur_s
-	(deg)	(deg)	–	(days)	(day)	(day)		(ppt)	(ppt)	(ppt)	(ppt)	(hr)	(hr)
1216203	273.4655	−5.2411	A	2.3247	3506.1242	3502.7167	0.47	126		67		5.8	5.3
			B	2.1994	3502.0225	3481.2407	0.45	69		30		3.1	5.2
Additional information: TGV-199, Gaia DR3 4173434534889039616, Tmag: 10.35, Teff:, Dist:													
Comments: only one sector available at the time of writing; PB in ASAS-SN													
3121385	138.6631	−39.0524	A	17.4925	3011.4576	3005.6961	0.33	122	117–126	78	75–89	4.6	4.7
			B	20.1544	2996.8688	3004.4404	0.62	146	141–149	133	125–148	6.1	4.4
Additional information: TGV-200, Gaia DR3 5430510714397083520, Tmag: 13.12, Teff:, Dist: 440 pc													
Comments: apsidal motion on both PA and PB; PA and PB in ASAS-SN													
20938739	233.0364	−4.5114	A	3.9561	2694.0852	2700.0188	0.50	171		158		4.4	4.5
			B	4.9446	2700.7489			22				5.5	
Additional information: TGV-201, Gaia DR3 4401400571324534016, Tmag: 9.44, Teff:, Dist: 345 pc													
Comments: from VSG and PHT[a] and EBP[b]; only one sector available at the time of writing													
Comments: PB may be slightly off; there may be B_{sec} but hard to tell													
26993740	356.2475	50.0971	A	1.8842	1766.4777	2854.5747	0.52	100	6–120	20		2.0	3.3
			B	9.2238	2854.965	2859.4045	0.52	54	44–142	17		3.0	2.5
Additional information: TGV-202, Gaia DR3 1943564205724787840, Tmag: 11.71, Teff:, Dist: 188 pc													
Comments: $T_0(B_{sec})$ may be slightly off; PA in ASAS-SN													
27258509	292.9677	9.8500	A	2.1253	2771.5387			47	43–55			2.7	
			B	17.7779	2770.1229	3526.9428	0.43	90	84–95	38	35–44	3.9	4.9
Additional information: TGV-203, Gaia DR3 4302472704155454592, Tmag: 13.09, Teff:, Dist: 1026 pc													
Comments: PA in ASAS-SN													
48089827	282.0706	51.2979	A	4.8637	3660.8489	3658.4146	0.50	140	101–154	115	89–131	3.8	3.6
			B	8.1718	3638.1317	3650.4113	0.50	97	88–121	72	57–93	4.3	4.2
Additional information: TGV-204, Gaia DR3 2144698898581885184, Tmag: 13.53, Teff:, Dist: 1383 pc													
Comments: dramatic ETVs with Pout 1400 d; PA and PB in ZTF													
48677841	299.3129	−14.1831	A	2.0582	3825.5941	2770.7586	0.50	73		23		4.2	3.9
			B	3.3182	3824.1794			23				3.5	
Additional information: TGV-205, Gaia DR3 6878567390734910208, Tmag: 10.68, Teff: 6356 K, Dist: 551 pc													
Comments: only one sector available at the time of writing; PA in ASAS-SN													

Note. The full table is available online.
TGV-N = TESS/GSFC/VSG quadruple candidate -N;
$T_{0,p/s}$ = Time of primary/secondary (in BJD-2,457,000); $Dep_{p/s}$ = Depth of primary/secondary; $Dur_{p/s}$ = Duration of prim/sec
ϕ_s = Secondary phase; Teff = Composite effective temperature; ppt = parts-per-thousand
$Dep_{p/s}$(spr) = Spread of nonblended primary/secondary eclipse depths across available sectors

(This table is available in its entirety in machine-readable form in the online article.)
[a] https://www.zooniverse.org/projects/nora-dot-eisner/planet-hunters-tess/talk/2112/2512585?comment=4121105&page=1
[b] https://www.zooniverse.org/projects/vbkostov/eclipsing-binary-patrol/talk/6324/3452938?comment=5820654&page=1

even confirm its higher-order multiplicity. The signal is often small and easy to miss, especially when the resulting "smear" in the lightcurve folded on the BLS period is difficult to notice during a visual inspection. The generalized functions mentioned above naturally account for this issue as they provide the time of minimum light for each individual eclipse, thus relaxing the requirement for strict periodicity between consecutive eclipses. An example of measured ETVs is shown in Figure 8 for the case of the quadruple candidate TIC 48089827.

3. The Catalog

The results presented here expand the TGV catalog with 52 new eclipsing quadruple star candidates, bringing the total number that we have published in K22, K24, and this work to 250. Each catalog entry provides detailed information about the target, including TIC and Gaia DR3 identifiers, sky position, TESS magnitude, measured ephemerides, primary and, where applicable, secondary eclipse depths and duration, and secondary phases. The orbital periods of the two component EBs are labeled as PA and PB, for simplicity ordered such that PA < PB. For completeness, we also incorporate Gaia DR3 distance estimates, composite effective temperature, and key astrometric measurements. Supplementary notes are provided where relevant, highlighting potential issues or interesting features. Finally, to ensure catalog consistency we have assigned each target a distinct TGV identifier, starting with TGV-199. To facilitate data analysis and further investigations, we have compiled the catalog's content into a machine-readable format, with the structure and organization highlighted in Table 1.

Figure 9 illustrates that most of the observed targets are close to the Galactic plane. This distribution aligns with the broader pattern observed in the TESS EB population (see

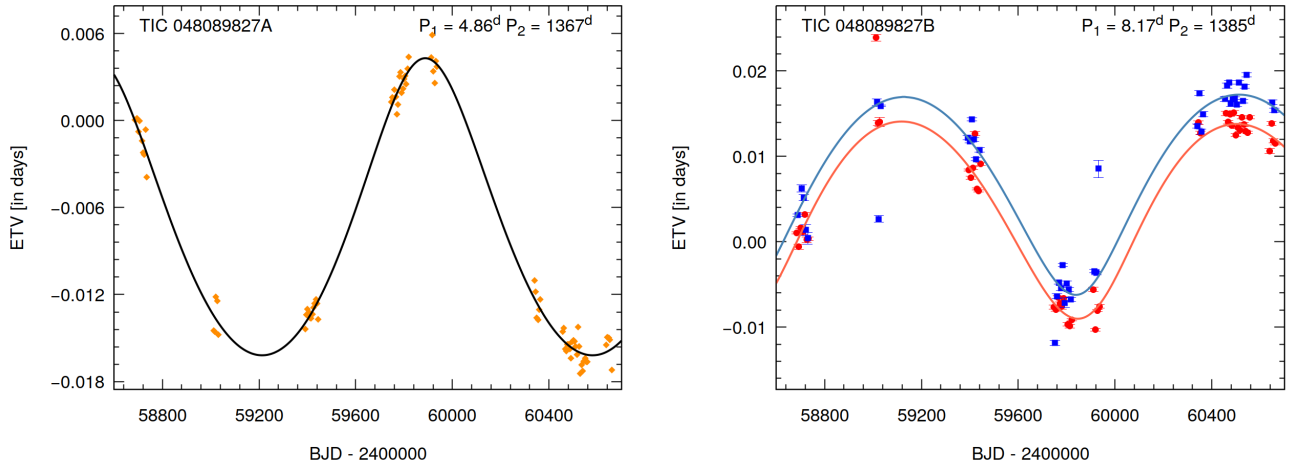

Figure 8. Measured anticorrelated ETVs for the PA ≈ 4.86 days component (left panel, average of primary and secondary eclipses) and PB ≈ 8.17days components (right panel, primary (red) and secondary (blue) eclipses) for TIC 48089827. The two EBs produce dramatic, anticorrelated ETVs that confirm the target as a genuine quadruple system. The solid curves represent the best-fit models indicating that the ETVs are dominated by the light travel-time effect, and suggesting an outer period of about 1400 days.

Figure 9 of V. B. Kostov et al. 2025) from which we are extracting these candidates. The 52 targets presented here encompass a range of TESS magnitudes, spanning from $T = 8.5$ mag (TIC 391461666) at the brightest end to $T = 15$ mag (TIC 359247237) for the faintest target. The average TESS magnitude is approximately 12.3, while the median is 12.7 mag. Thirty out of the 52 targets have effective temperatures provided by Gaia DR3. These range from 4500 K for TIC 165052445 to the notable outlier of 23,000 K for TIC 277316707, with mean/median values of 7700/6700 K, respectively.

To assess the likelihood of the 52 candidates being genuine gravitationally bound quadruples, we investigated several Gaia DR3 indicators commonly associated with potentially unresolved multiplicity: `astrometric_excess_noise` (AEN), `astrometric_excess_noise_sig` (AENS), renormalized unit weight error (RUWE) systems, and `non_single_star` (NSS; e.g., V. Belokurov et al. 2020; Z. Penoyre et al. 2020; K. G. Stassun & G. Torres 2021; P. Gandhi et al. 2022; D. M. Rowan et al. 2023). Overall, there are AEN/AENS/RUWE measurements for 49/49/46 targets, respectively. As highlighted in Figure 9, the vast majority of AENS values are enormous, with 47/45/28 targets showing AENS higher than 3/5/100, respectively. Approximately 40% of the candidates demonstrate AEN values greater than 1 mas, with the top five targets having AEN in excess of 10 mas and AENS surpassing 70,000. The most dramatic case is TIC 139995365—a well-isolated target with hardly any contamination from nearby sources—where AEN and AENS are ≈89 mas and ∼10 million, respectively.

In terms of RUWE, the values are greater than 1.4—a typically considered threshold for the presence of unresolved companions (e.g., K. G. Stassun & G. Torres 2021)—for 28 of the 52 targets. Additionally, four targets have nonzero NSS values: TIC 258507555 (NSS = 1), TIC 412074304 (NSS = 2), TIC 430752710 (NSS = 2), and TIC 466310009 (NSS = 2). The corresponding AEN, AENS, and RUWE are in the range of 0.1–1.3 mas, 22–2585, and 1–8.1, respectively; TIC 258507555 and TIC 466310009 are discussed in further detail below. These considerations suggest that a potentially significant fraction of the 52 quadruple candidates presented here may indeed be genuine quadruple systems of two EBs orbiting the common center of mass and observed in motion thanks to Gaia's precise astrometric measurements.

3.1. Period, Eclipse Depth, and Duration Distributions

The orbital periods of the individual components in a 2+2 quadruple star are one of the fundamental properties describing the system. These act as critical tracers of its formation history and key factors for predicting its evolution: for example, theoretical models of resonant capture in 2+2 quadruples indicate that while period ratios of 1:1 should be rare due to the inefficiency of the mechanism, period ratios of 3:2 and 2:1 are expected to be relatively common (S. Breiter & D. Vokrouhlický 2018; S. Tremaine 2020). Although determining such ratios is generally challenging, eclipsing quadruple systems represent ideal targets to do so, and indeed several recent studies have leveraged various photometric datasets to directly measure periods for hundreds of these systems (e.g., P. Zasche et al. 2019, 2022; P. Zasche 2024; P. Zasche et al. 2025; K22, K24).

In Figure 10 we show the measured periods PA and PB for each of the 52 systems presented here. Overall, these findings are in line with the results of K22 and K24. Specifically, granted the number of targets is relatively small, we find no exact 1:1, 3:2, and 2:1 period ratios. Only four systems are within 1% of low-order integer ratios: TIC 229652559 (PB/PA = 1.005), TIC 122124665 (PB/PA = 1.51), TIC 20938739 (PB/PA = 1.249), and TIC 122994468 (PB/PA = 1.24); TIC 430752710 is within 5% of 2:1 (PB/PA = 2.05). For the systems that produce significant secondary eclipses, we measure the corresponding depths and duration, and estimate the respective $e\cos(\omega)$ and $e\sin(\omega)$. These are illustrated in the upper panels of Figure 11, showing that most of the component EBs have nearly circular orbits, and the secondary versus primary depth ratios are mostly evenly distributed between 0 and 1. For completeness, in Figures 9, 10, and 11 we also show the basic parameters and orbital properties of all 250 TGV quadruple candidates.

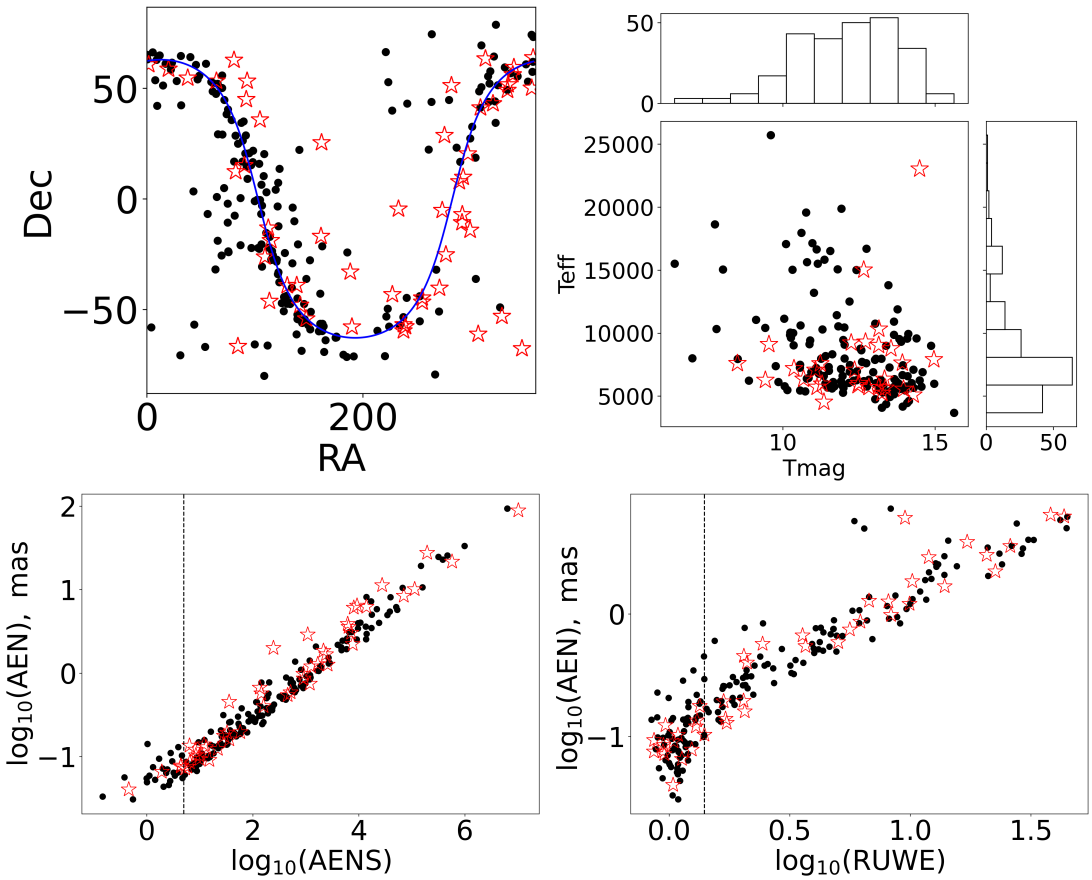

Figure 9. Upper left panel: sky position in R.A. and decl. for the 52 quadruple candidates presented here (red stars). The black dots represent the other 198 targets in the TGV catalog, and the blue line represents the Galactic plane. Upper right: corresponding Gaia DR3 composite effective temperature as a function of TESS magnitude. Lower panels: Gaia DR3 astrometric excess noise (AEN), astrometric excess noise sig (AENS), and renormalized unit weight error (RUWE); AEN and AENS are in units of milliarcsec. Note the axes are in log10 base. The dashed vertical line in the right panel represents RUWE = 1.4, a potential indicator for unresolved companions.

3.2. Discussion

The chance geometric orientation required for binary stars to produce eclipses make these relatively rare. Indeed, of the hundreds of millions of stellar binaries spread across the entire sky (some of which have been monitored for centuries), only a relatively small number—several million—have the appropriate orbital configuration to be confirmed as eclipsing thanks to observations from ASAS-SN, ATLAS, CoRoT, Gaia, Kepler, OGLE, TESS, and ZTF (e.g., N. Mowlavi et al. 2023; D. M. Rowan et al. 2023; V. B. Kostov et al. 2025, and references therein). A tiny fraction of these—less than a thousand at the time of writing—have been found to be, in fact, eclipsing triple- and higher-order candidates for stellar multiples (e.g., T. Borkovits 2022, and references therein). It is worth pointing out that this roughly speaking one in a hundred chance to see, e.g., tertiary eclipses in 2+1 triples or eclipses from both EBs in 2+2 quadruples is only a lower limit. The probability of detecting such systems is highly dependent on their overall architecture—which is practically unknown a priori—and thus the fraction of EBs in noneclipsing higher-order multiples is likely much higher (e.g., A. Tokovinin 2021).

It is essential to clarify that the 250 targets listed in our full TGV catalog do not signify an exhaustive inventory of eclipsing 2+2 quadruples identified in TESS data. Rather, they represent our best effort to compile a sample of candidates that pass thorough scrutiny against false positives as possible. Naturally, it is certainly possible there are yet more candidates hidden in the data. However, based on our experience we would be surprised if these still-undiscovered stellar gems number in the hundreds as members of the VSG have already conducted visual inspections of millions of TESS EB lightcurves and identified thousands of potential candidates. Most of these, however, did not pass our vetting and validation criteria. Thus, while a comprehensive study of completeness and reliability is beyond the scope of this work, to facilitate future investigations we provide in Table 2 a representative sample of ∼500 candidates for eclipsing quadruples that failed two common tests: (i) photocenter motion during eclipse and (ii) resolved field star that cannot be definitively ruled out as an unrelated EB based on TESS data alone.

3.2.1. Interesting Systems

Below we list several systems exhibiting interesting features in addition to the two sets of detected eclipses.

1. *TIC 48089827 (TGV-204).* TESS observed TIC 48089827 in 15 sectors (14, 15, 26, 40, 41, 53, 54, 55, 59, 75, 79, 80, 81, 82, and 86), providing an excellent baseline for long-term ETV measurements. The target produced two sets of eclipses with PA ≈ 4.86 days and PB ≈ 8.17 days, the latter exhibiting primary and

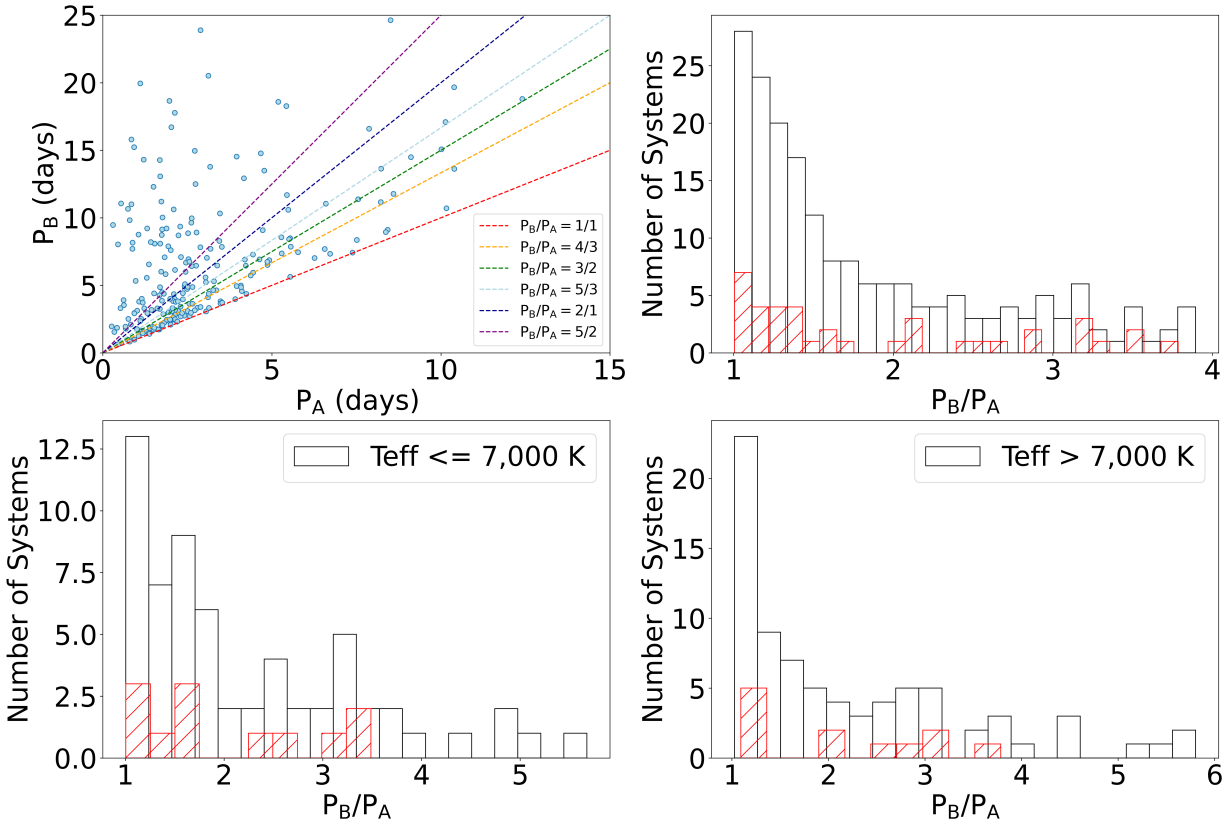

Figure 10. Upper left panel: measured periods of the A and B binaries of all 250 quadruple candidates in the TGV catalog, compared to several integer ratios of PB/PA. Upper right panel: corresponding period ratios PB/PA, such that PA < PB. The black histogram represents all 250 targets in the TGV catalog, and the red histogram—the 52 presented here. Lower panels: same as upper right panel but separated for targets with Teff <7000 K (left) and Teff >7000 K (right). The panels are meant for comparison with Figure 16 from P. Zasche et al. (2023).

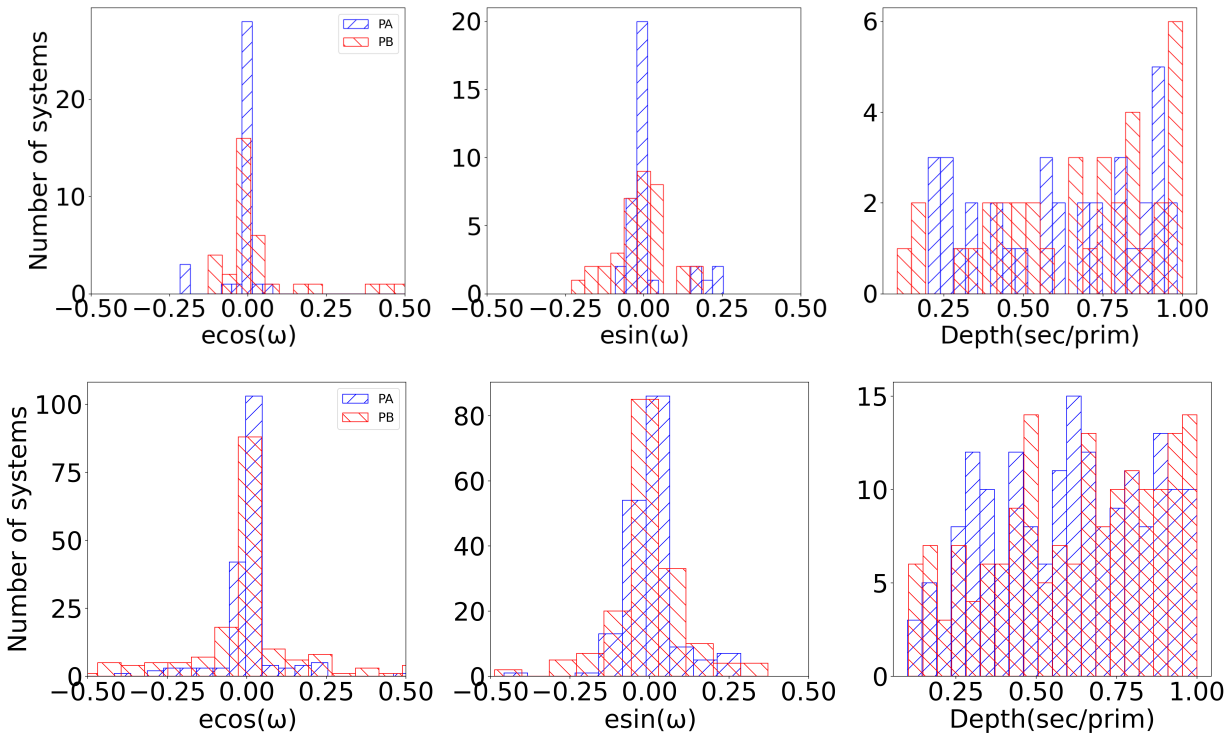

Figure 11. Upper left and middle panels: measured $e\cos\omega$ and $e\sin\omega$ for the 52 quadruple candidates presented here. Upper right panel: measured secondary-to-primary eclipse depths. The blue/red colors in the lower panels correspond to binary A/B, respectively. Lower panels: same as upper panels, but for all 250 TGV quadruple candidates.

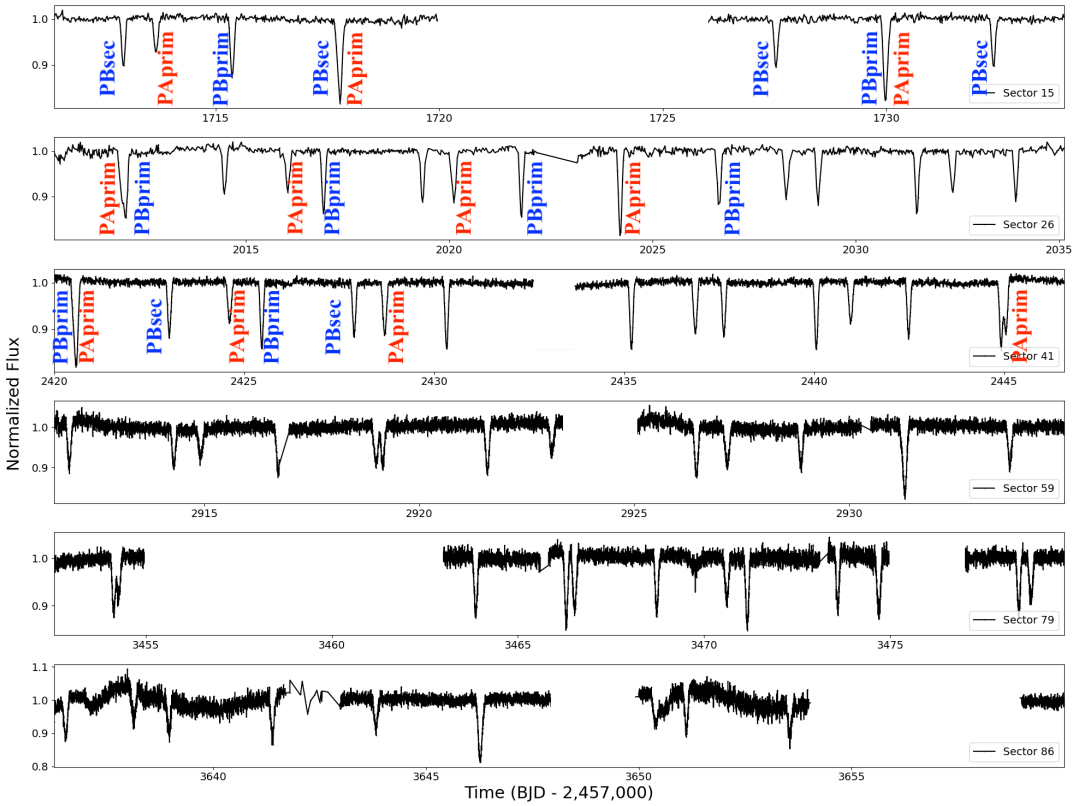

Figure 12. Same as Figure 1 but illustrating 6 sectors of TESS data (out of 15 total) for TIC 48089827.

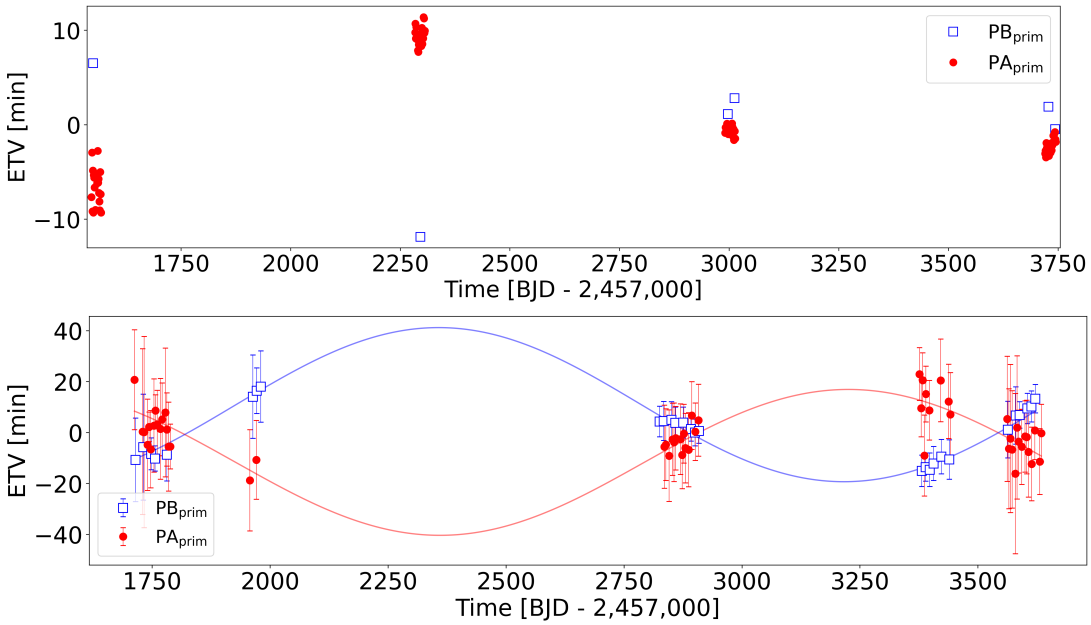

Figure 13. Same as Figure 8 but for TIC 289822938 (upper panel) and TIC 352830705 (lower panel). Both targets produce prominent anticorrelated ETVs, although the sparse coverage makes estimating the outer period difficult. For illustrative purposes, the lower panel shows a double sine fit to TIC 352830705 with a potential outer period of about 1700 days.

secondary eclipses. The corresponding eclipses are often partially or fully blended, as shown on Figure 12. As demonstrated in Figure 8, the two EBs show dramatic, anticorrelated ETVs—the signature effect of light travel-time (e.g., H. Frieboes-Conde & T. Herczeg 1973; T. Borkovits et al. 2016). This confirms TIC 48089827 as a gravitationally bound eclipsing quadruple star. For illustrative purposes, we fit a simple model to the measured ETVs and estimated an outer period of about 1400 days. This is the longest confirmed outer period in the TGV catalog.

2. *TIC 289822938 and TIC 352830705.* TESS observed TIC 289822938 (TGV-233) in Sectors 9, 36, 62, and 89, where the target produced two sets of eclipses with PA ≈

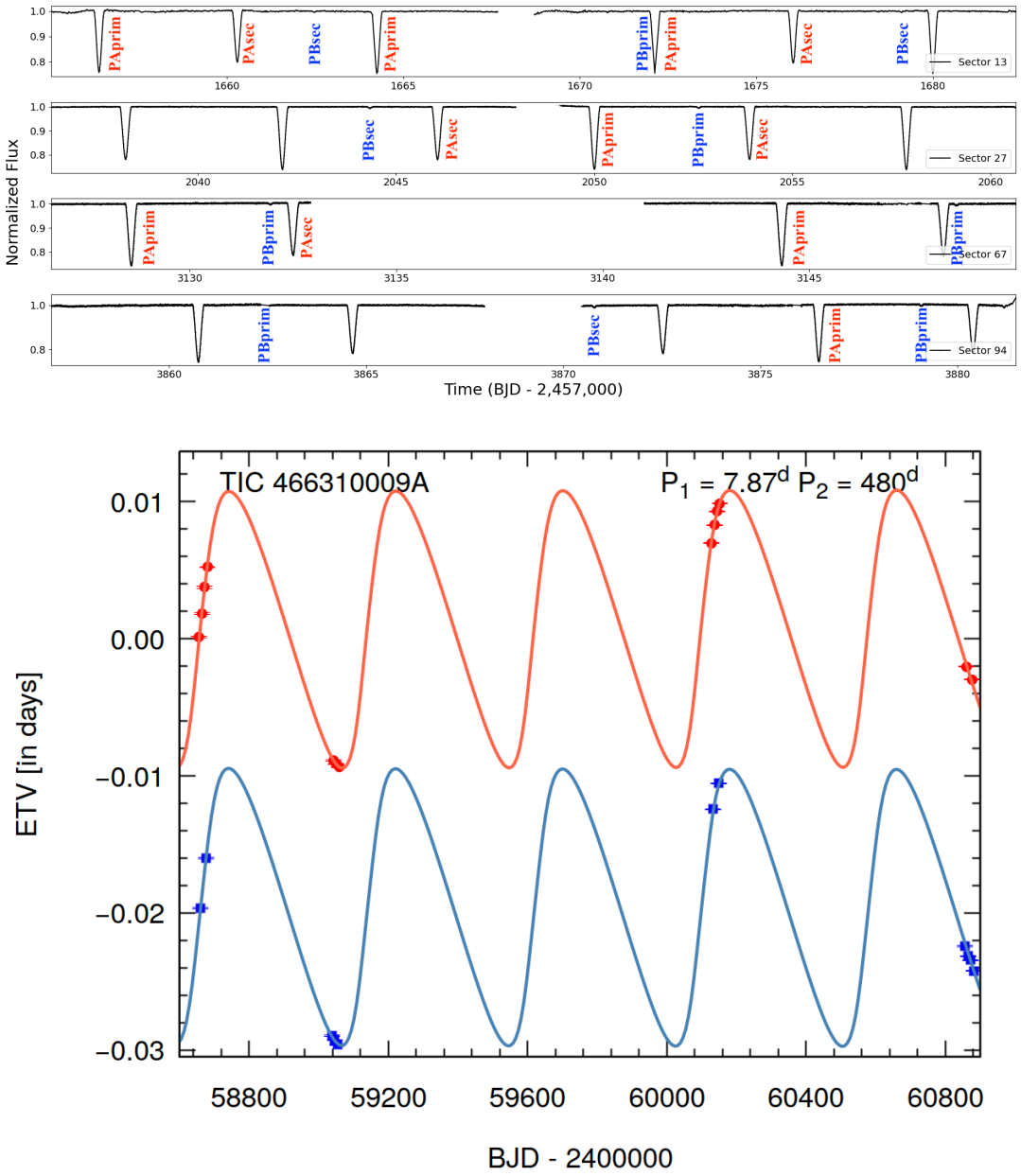

Figure 14. Upper panels: same as Figure 12 but for TIC 466310009. The lower panel shows a preliminary analytic light travel-time effect and dynamical effect fit to the primary (red) and secondary (blue) eclipses of PA. The model indicates an outer period of about 480 days, consistent with Gaia.

0.92 days and PB $\approx$ 15.24 days. As illustrated in Figure 13, the corresponding ETVs show clear anticorrelated modulations between the two primary eclipses. Like the case of TIC 48089827, this practically confirms the physically bound quadruple nature of TIC 289822938.

TIC 352830705 (TGV-238) was observed in 13 sectors and produced two EBs with PA $\approx$ 3.44 days and PB $\approx$ 8.29 days. Like TIC 48089827 and TIC 289822938, the two EBs exhibit prominent anticorrelated ETVs consistent with a light travel-time effect around the common center of mass, confirming the target as a genuine 2 + 2 quadruple system.

The ETV coverage for both of these targets is rather sparse, making robust measurements of the outer period difficult. For illustrative purposes, we fit a double sine model to TIC 352830705, and estimated a potential outer period of about 1700 days.

3. *TIC 466310009 and TIC 258507555.* TESS observed TIC 466310009 (TGV-249) in Sectors 13, 27, 67, and 94, and produced two sets of eclipses with periods PA $\approx$ 7.87 days (deep) and PB $\approx$ 16.6 days (much shallower). As seen from Figure 14, PA shows nonlinear primary and secondary ETVs; the PB eclipses are too few for meaningful ETV measurements. Upcoming TESS observations in Sectors 101, 102, 103, and 104 will help further constrain the architecture of the system.

As illustrated in Figure 15, TIC 258507555 (TGV-229) was observed in Sectors 19, 60, and 73, and produced two sets of eclipses with periods PA $\approx$ 0.87 days (shallower) and PB $\approx$ 7.7 days (much deeper). The target was close to the detector edge in Sector 19 and the data

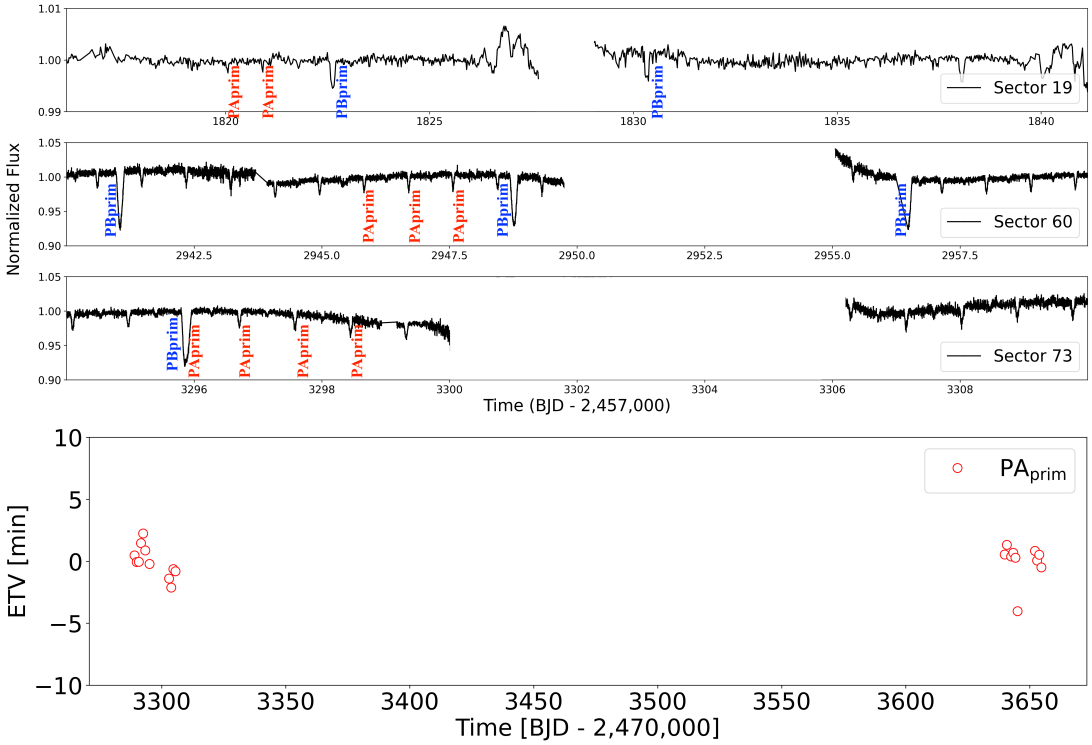

Figure 15. Upper panels: same as Figure 14 but for TIC 258507555. Large sections of the lightcurve are dominated by systematics, especially in Sector 19 when the target is close to the detector edge. Lower panel: same as Figure 8 but for TIC 258507555. There are no indications for significant ETVs on PA. Here, Gaia measured an outer period $P_{out} \approx 277$ days and eccentricity $e_{out} \approx 0.1$. The ETVs in TESS are too sparse to estimate the orbital period.

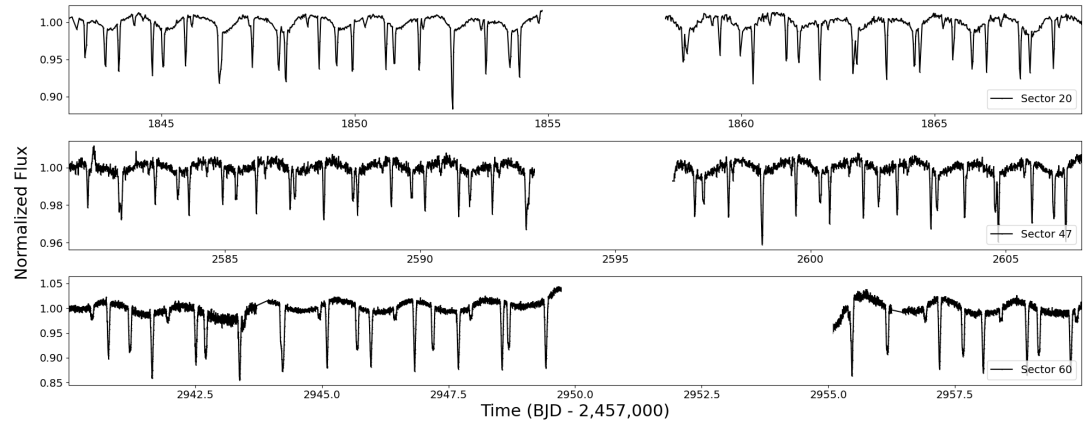

Figure 16. TESS FFI eleanor lightcurve of the 2+2 quadruple candidate TIC 165052445. A resolved nearby star (separation of about 3.″8), TIC 741891699, has similar parallax and proper motion to the target, suggesting the two may be a potentially comoving wide quintuple. The apparent depth changes in both sets of eclipses are systematic in nature, due to contamination from TIC 165052447 (∼3 pixels away and ∼2 mag brighter).

are rather poor; a substantial portion of Sector 73 is strongly affected by systematics as well. Overall, there are no indications for significant ETVs on PA (see Figure 15, lower panel); PB has too few eclipses for meaningful measurements.

Interestingly, TIC 258507555 and TIC 466310009 are not only flagged as non-single-stars by Gaia, but even have fully resolved astrometric outer orbits. This essentially confirms that both candidates are indeed gravitationally bound quadruple systems with relatively compact outer orbits. TIC 258507555 has an outer period $P_{out} \approx 277$ days, relatively small outer eccentricity $e_{out} \approx 0.1$, and inclination of $i_{out} = 86.6 \pm 1.3$ deg; the outer orbit for TIC 466310009 has a period of $P_{out} \approx 474$ days, an eccentricity of $e_{out} \approx 0.5$, and inclination of $i_{out} = 90.2 \pm 1.2$ deg. While a comprehensive analysis of these two systems is beyond the scope of this work, the measured PA ETVs of TIC 466310009 are qualitatively consistent with Gaia's orbit as highlighted in Figure 14.[24] As a test, we fitted a preliminary analytic model based on Roemer's delay (or light travel-time

[24] TIC 258507555 produced too few eclipses for meaningful ETV constraints on the outer orbit.

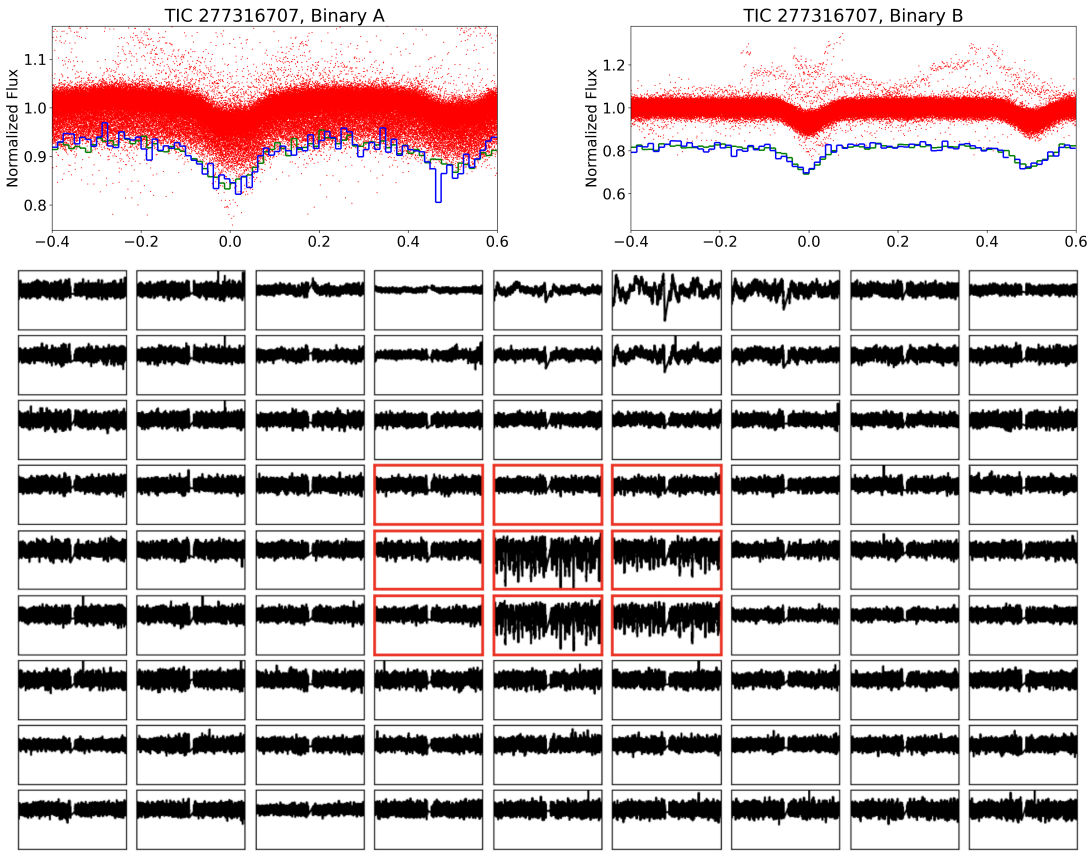

Figure 17. Upper panels: phase-folded TESS (red) and ASAS-SN data (green and blue, for the corresponding g and V bands) for quadruple candidate TIC 277316707. We measured orbital periods for the two EB components of PA = 1.475034 days (left, compared to 6.965 days as reported by L. W. IJspeert et al. 2021) and PB = 1.93217 days (right, consistent with L. W. IJspeert et al. 2021). Lower panels: 11 × 11 pixel-by-pixel lightcurves centered of the target for Sector 27. The red contours represent the ELEANOR aperture used to extract the lightcurve. We do not see a 6.965 day signal in the pixels surrounding the target.

effect, LTTE) and dynamical effect (DE; e.g., T. Borkovits et al. 2015, 2016) to the PA primary and secondary ETVs, assuming a coplanar outer orbit. The model suggests that the DE is about three times larger than the LTTE, and indicates an outer period of about 480 days, in line with Gaia, as well as component masses of 3.5 $M_{\odot}$ for binary A, and 1.0 $M_{\odot}$ for binary B, respectively, albeit with considerable uncertainty.

4. *TIC 165052445 (TGV-225).* TIC 165052445 is a known EB observed by TESS in Sectors 20, 47, and 60. As illustrated in Figure 16, the target produced two sets of eclipses with periods PA ≈ 1.49 days and PB ≈ 1.73 days, the latter identified as part of the HAT survey (J. D. Hartman et al. 2011). As mentioned in Table 2, both EBs are detected in ASAS-SN and ZTF data (also see the discussion below), strengthening our interpretation of TIC 165052445 as a bona fide quadruple system. Additionally, there is a resolved nearby star, TIC 741891699, at a projected separation of about 3.″8, which is much too faint to produce either EB as contamination. Interestingly, TIC 165052445 and TIC 74189169 have similar enough parallax (9.13 ± 0.03 mas versus 9.07 ± 0.09 mas) and proper motion ($\mu_{\rm R.A.} = 61.38 \pm 0.03$ mas yr^{-1} versus $\mu_{\rm R.A.} = 59.83 \pm 0.09$ mas yr^{-1}; $\mu_{\rm decl.} = -63.67 \pm 0.02$ mas yr^{-1} versus $\mu_{\rm decl.} = -61.46 \pm 0.09$ mas yr^{-1}) that the two likely represent a wide comoving quintuple system with a (2+2)+1 hierarchical configuration.

Table 3
Eclipsing Quadruple Star Candidates Brighter Than Tmag = 12 and Primary Eclipses Deeper Than 1% for At Least One of the Component EBs

TIC	Tmag	Depth$_{\rm A}$ (%)	Depth$_{\rm B}$ (%)
391461666	8.52	17	4
99875938	9.43	13	3
20938739	9.44	17	2
52877118	9.55	18	16
79908874	10.15	3	2
297251275	10.18	15	3
1216203	10.35	7	12
130946041	10.40	11	0.6
139995365	10.42	11	26
79062805	10.46	2	32
466310009	10.47	25	0.6
48677841	10.68	7	2
430752710	11.08	5	3
258507555	11.13	2	6
412074304	11.24	1	3
286779918	11.30	27	0.5
165052445	11.35	4	7
26993740	11.71	10	5

5. *TIC 277316707 (TGV-231).* L. W. IJspeert et al. (2021) reported TIC 277316707 as an eclipsing quadruple candidate with $P1 = 1.93217$ days and $P2 = 6.965$ days. We independently discovered the target and during our

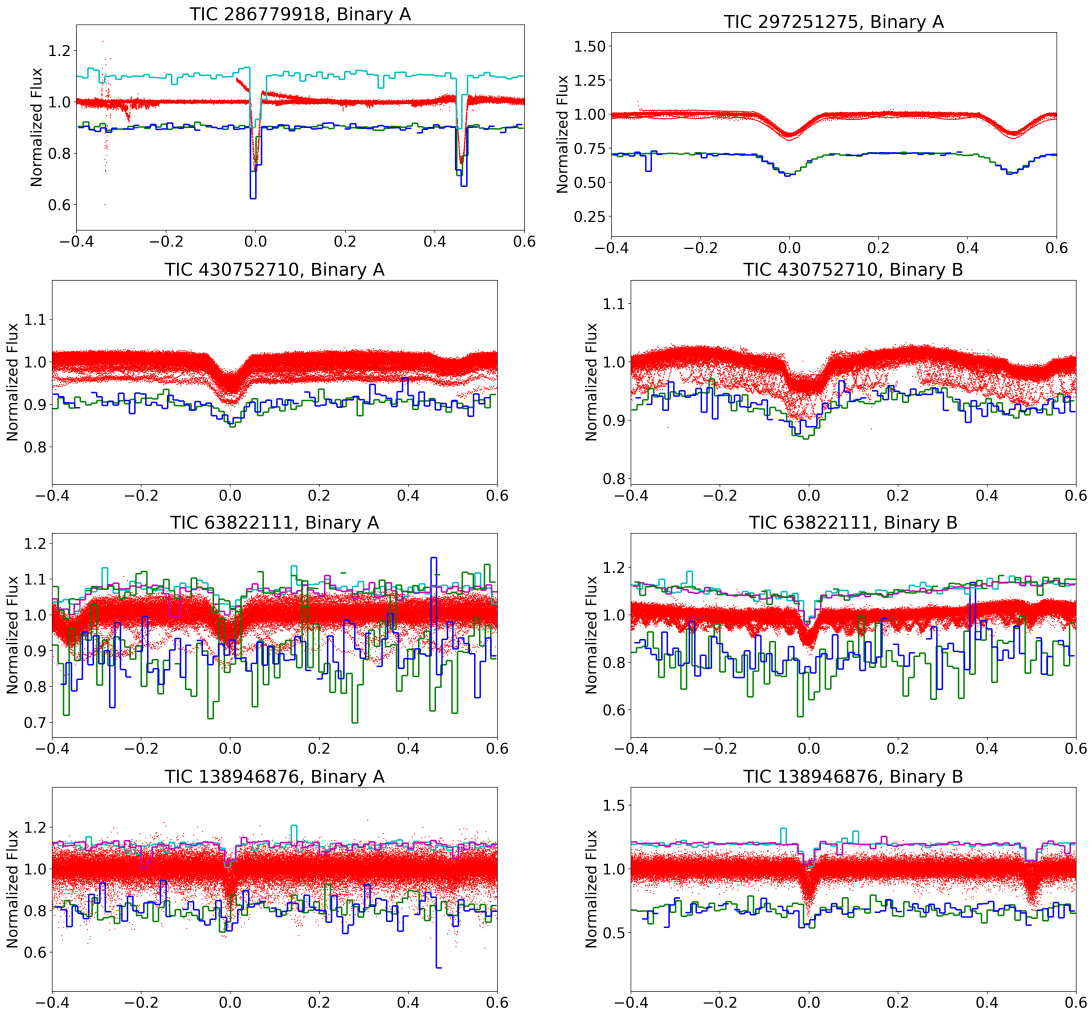

Figure 18. Comparison between TESS (red), ASAS-SN (green and blue), and ZTF (cyan, magenta, and green, for the zg, zr, and zi bands, respectively) photometry for the several quadruple candidates. The ground-based photometry is binned for clarity. First row: both primary and secondary eclipses seen for one component of the respective quadruple candidate. Second row: both primary and secondary seen for both components. Third row: both EBs are present in ZTF but neither in ASAS-SN. Last row: both EBs present in ZTF but only one or the other in ASAS-SN.

analysis of the system noticed that P2 reported by L. W. IJspeert et al. (2021) is incorrect. As highlighted in Figure 17, the correct value from TESS is $P2 = 1.475034$ days (corresponding to PA in this catalog). We confirmed this value with photometry from ASAS-SN, where both sets of eclipses are clearly visible in the phase-folded data. The correct P2 period is not a low-integer ratio of 6.965 ($6.965/1.475034 \approx 4.7$), suggesting that the latter is potentially a different signal. We searched for such a signal in the pixel-by-pixel light-curves of a 11×11 TESS pixel image at the center of the target but could not find evidence for it. Thus, we consider TIC 277316707 as a new quadruple candidate and include it in the TGV catalog presented here.

6. *Bright candidates with deep eclipses.* New observations of the quadruple candidates presented here can help confirm their nature and constrain the underlying orbital configuration. These observations can include obtaining new eclipse times, measuring radial velocities, and directly resolving the individual components through high-resolution imaging. To assist such potential investigations, we provide in Table 3 a list of relatively bright systems ($T \leqslant 12$ mag) with eclipses deeper than 1%.

3.3. Comparison with Archival Data

In the context of eclipsing binary stars and transiting exoplanets it is not unreasonable to consider as "archival" observations with data that extend back in time on the order of decades (and more). Interestingly, TESS is already reaching the lower limit of this working definition, observing continuously for more than 7 yr and still going strong (G. R. Ricker et al. 2015). As demonstrated here and in other works, the synergy of ever-increasing baseline and high-precision photometry provides sensitivity to years-long period changes in eclipsing multiple stellar systems (e.g., T. Borkovits et al. 2025). To investigate even longer-term timescales, we searched the ASAS-SN SkyPatrol,[25] DASCH,[26] and ZTF[27] databases.

Before discussing the results from this search, we would like to note two important considerations. Specifically, the ASAS-SN and ZTF pixel scales (8″ and 1″, respectively) are much smaller than that of TESS (21″) and so is the potential

[25] http://asas-sn.ifa.hawaii.edu/documentation/index.html
[26] https://daschlab.readthedocs.io/en/latest/
[27] http://atua.caltech.edu/ZTF/Zubercal.html

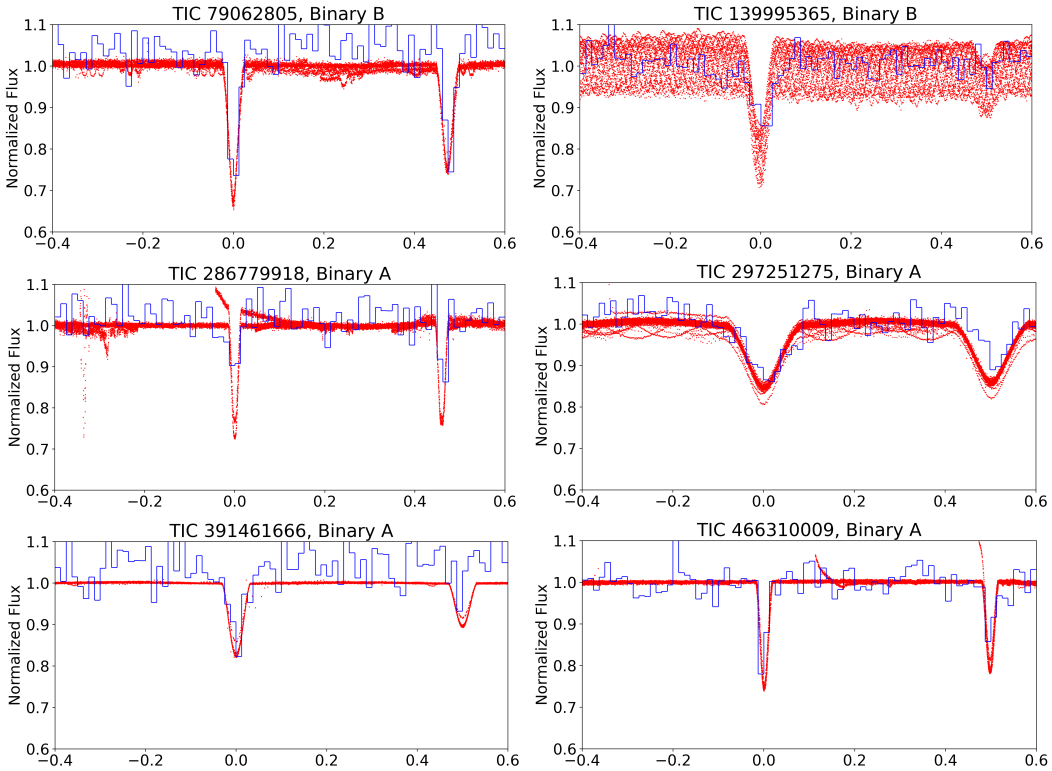

Figure 19. Same as Figure 18 but showing a comparison between TESS (red) and DASCH (blue) for the six targets where the TESS eclipses are seen in DASCH. There are no indications of dramatic depth changes or apsidal motion of century-long timescales.

contamination from nearby sources. Thus, detecting two sets of eclipses for a particular target in either of the ground-based datasets dramatically strengthens the quadruple interpretation of the system. With that said, the observational cadence of the ASAS-SN and ZTF photometry is relatively low compared to TESS, and it is not unlikely for the first two to miss some (and potentially even all) eclipses seen in the latter. Therefore, not detecting these in the archival data does not rule out the quadruple candidate.

Our cross-match query returned lightcurves for 46, 54, and 25 targets from ASAS-SN, DASCH, and ZTF, respectively. Of these, we found that at least one of the component EBs is unambiguously detected in the phase-folded ASAS-SN data in 39 out of the 46 lightcurves, and both EBs can be seen in 16 lightcurves. ZTF detects at least one of the EBs in 21 out of the 25 lightcurves and both EBs in 14 out of the 25 lightcurves. We note that some of these eclipses are present in one of the datasets but not in the other, such that at least one EB is present in the ground-based photometry for 46 unique targets. Figure 18 highlights the successful recovery of (i) the primary and secondary eclipses for binary A of TIC 286779918 and TIC 297251275; (ii) both EBs of TIC 430752710; (iii) both EBs of TIC 63822111 in ZTF but neither in ASAS-SN; and (iv) both EBs of TIC 138946876 in ZTF but only one of them in ASAS-SN. Overall, we find consistency between the periods in all datasets to within the statistical uncertainties.

The eclipses of six targets are quite clear in DASCH data: TIC 79062805 (binary B), TIC 139995365 (binary B), TIC 286779918 (binary A), TIC 297251275 (binary A), TIC 391461666 (binary A), and TIC 466310009 (binary A). Overall, all six EBs seem to be keeping pace between TESS and DASCH (see Figure 19), showing no indications of dramatic apsidal motion dramatic or eclipse depth variations on century-long timescales. The latter is in line with the nearly edge-on outer orbit of TIC 466310009, where despite the short outer period, high eccentricity, and strong dynamical interactions between the two components, binary A continues to produce eclipses for decades.

Finally, for completeness we also cross-matched our candidates against APOGEE spectroscopic binaries listed in M. Kounkel et al. (2021). None of our targets appear in the catalog as either SB3 or SB4.

4. Summary

We have presented the second expansion of our TESS/GSFC/VSG (TGV) catalog, adding 52 new candidates for eclipsing quadruple star systems. The results from this work bring the total TGV tally to 250 and represent our efforts to provide to the community a curated set of uniformly vetted, validated, and characterized hierarchical 2+2 systems discovered in TESS FFI data by sophisticated machine learning and highly trained volunteers. All targets passed extensive scrutiny, including photocenter measurements, ephemerides determination, and cross-match with available ground-based photometry. Each candidate exhibits two distinct sets of eclipses, all originating within ∼0.1–0.2 pixels (∼2″–4″) of the target; there are no resolved stars within said separation that are bright enough to be the source of either set. For each target, the catalog provides identifying information, measured ephemerides, eclipse depths, and durations, as well as relevant notes and comments. Several targets display pronounced

eclipse timing variations (ETVs), indicating dynamical interactions between the two eclipsing binary components; the ETVs for one system complete a ∼1400 day outer orbit during TESS observations. Many of the candidates exhibit notable astrometric excess noise and high renormalized unit weight error in Gaia measurements, suggesting detectable astrometric motion in a wider quadruple configuration. Two targets, TIC 258507555 and TIC 466310009, have complete orbital solutions from Gaia for the outer orbits. The former has an outer period of about 278 days, placing it among the top five most compact quadruples, and the latter is nearly edge-on with an outer inclination of $\approx 90.^{\circ}2$.

Acknowledgments

This paper includes data collected by the TESS mission, which are publicly available from the Mikulski Archive for Space Telescopes (MAST; STScI 2018). Funding for the TESS mission is provided by NASA's Science Mission directorate.

Resources supporting this work were provided by the NASA High-End Computing (HEC) Program through the NASA Center for Climate Simulation (NCCS) at Goddard Space Flight Center.

This research has made use of the Exoplanet Follow-up Observation Program website, which is operated by the California Institute of Technology, under contract with the National Aeronautics and Space Administration under the Exoplanet Exploration Program.

V. B. K., J.O., and W.W. are grateful for financial support from NSF grant AST-2206814. V.B.K. acknowledges support from NASA grants 80NSSC21K0631 and 80NSSC23K0270. T.B. acknowledges the financial support of the Hungarian National Research, Development and Innovation Office—NKFIH grant K-147131. T.B. acknowledges the funding from the HUN-REN Hungarian Research Network. G.H. thanks the Polish National Center for Science (NCN) for financial support through grant 2021/43/B/ST9/02972.

This work has made use of data from the European Space Agency (ESA) mission Gaia (https://www.cosmos.esa.int/gaia), processed by the Gaia Data Processing and Analysis Consortium (DPAC, https://www.cosmos.esa.int/web/gaia/dpac/consortium). Funding for the DPAC has been provided by national institutions, in particular the institutions participating in the Gaia Multilateral Agreement.

Facilities: Gaia, MAST, TESS, ASAS-SN, FLWO:1.5m, PO:1.2m.

Software: `Astropy` (Astropy Collaboration et al. 2013, 2018, 2022), `Eleanor` (A. D. Feinstein et al. 2019), `IPython` (F. Pérez & B. E. Granger 2007), `Keras` (F. Chollet et al. 2015), `LcTools` (A. R. Schmitt et al. 2019; A. Schmitt & A. Vanderburg 2021), `Lightcurve-factory` (T. Borkovits et al. 2013; S. Rappaport et al. 2017; T. Borkovits et al. 2018), `Lightkurve` (Lightkurve Collaboration et al. 2018), `Matplotlib` (J. D. Hunter 2007), `Mpi4py` (L. Dalcin et al. 2008), `NumPy` (C. R. Harris et al. 2020), `Pandas` (W. McKinney 2010), `Scikit-learn` (F. Pedregosa et al. 2011), `SciPy` (P. Virtanen et al. 2020), `Tensorflow` (M. Abadi et al. 2015), `Tess-point` (C. J. Burke et al. 2020).

Appendix A
Quadruple Candidates with Sparse Eclipses

Some of the targets presented here were flagged by members of our team as worthy of further investigations quite early in the TESS mission. At the time, the number of available sectors was small and so was the number of interesting features in the corresponding lightcurves. Several EBs produced a single extra transit-like event, quickly confirmed to be on-target through photocenter measurements, that could be interpreted as potentially due to a circumbinary planet. Naturally, this was quite an exciting possibility as such planets are few and far between. As TESS continued observing, however, the events repeated in a strictly periodic pattern indicating they are in fact produced by a second EB with an orbital period (much) longer than a TESS sector.

One of the more illustrative examples of this situation is TIC 391461666 (TGV-241), where the lightcurve shows an EB with PA ≈ 3.08 days and one extra transit/eclipse-like event in each of the three sectors the target was observed in (Sectors 14, 41, and 54). The three events are similar in depth, duration, and overall shape, and are separated by hundreds of days (see Figure A1). Specifically, the first and the second are about 742.7 days apart, while the second and the third are separated by about 351.8 days. Assuming the three events are the same eclipse, the gaps between them are too large to uniquely determine the period of the EB, with multiple integer ratios of $P(N) = 351.8/\mathrm{N}$ days producing viable phase-folded lightcurves. The two most promising options seem to be for $P(9) = 39.09$ days (i.e., $N = 9$), and $P(18) = 19.54$ days (i.e., $N = 18$), both producing a convincing phase-folded lightcurve (see upper panels, Figure A2). While all other values of N between 7 and 20 can be ruled out from the available data (see lower panels, Figure A2), smaller values of $N = 2$–6 would also work. It is also possible that the three events represent two primary and one secondary eclipse. Alas, TESS will not observe TIC 391461666 again and we cannot confirm PB at the time of writing. Nevertheless, the target is likely an eclipsing 2+2 quadruple and is thus included in the catalog presented here.

Another example is TIC 286779918 (TGV-232), which produced six additional eclipse-like events (in addition to the much deeper EB, see Figure A3). The two pairs of extra events in Sectors 59 and 73 have practically the same separation between the events of ∼16.125 days, suggesting that the pairs are potentially related. However, a period of ∼16.125 days does not produce a consistent phase fold of the entire lightcurve Instead, assuming the two pairs have the same origin, we can speculate that they are primary and secondary eclipses separated by $\mathrm{PB}(N) \approx 381/N$ day periods between Sectors 50 and 73. Overall, three of the events fold well on a period of PB ≈47.6 days (i.e., $N = 8$) and PB ≈ 23.81 days (i.e., $N = 16$;see upper panels, Figure A4). Another two events fold well on said periods for Sectors 59 and 73, and potentially 19 if another event is assumed to blend with the deep PA eclipse—but the event from Sector 86 does not. Like the case for TIC 391461666, the available data allows ruling out several values of N. Altogether, this indicates that the six events may not have a common origin and suggests that the above assumption is likely incorrect. Thus, we cannot confirm PB from the available TESS data at the time of writing. With that said, the clear periodicity of ∼16.125 days strongly suggests a second EB, justifying the inclusion of TIC

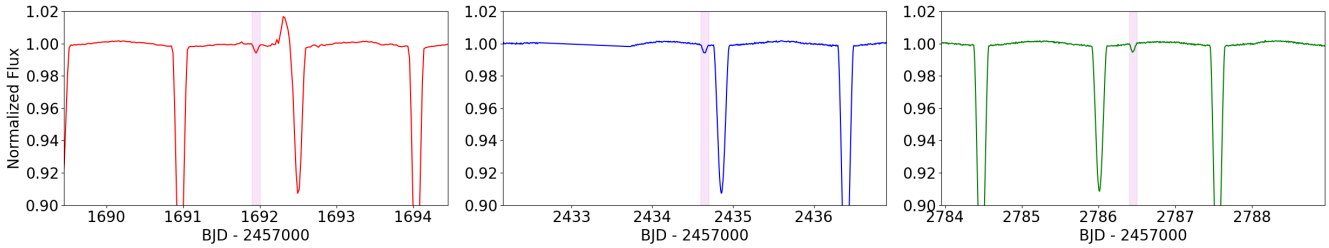

Figure A1. TESS FITSH lightcurve of TIC 391461666 for Sectors 14 (left), 41 (middle), and 54 (right), highlighting the three transit/eclipse-like event. The period of the second EB, PB = 351.8/N days, where N is an integer value, cannot be uniquely determined at the time of writing due to the large separation between the three eclipses it produces.

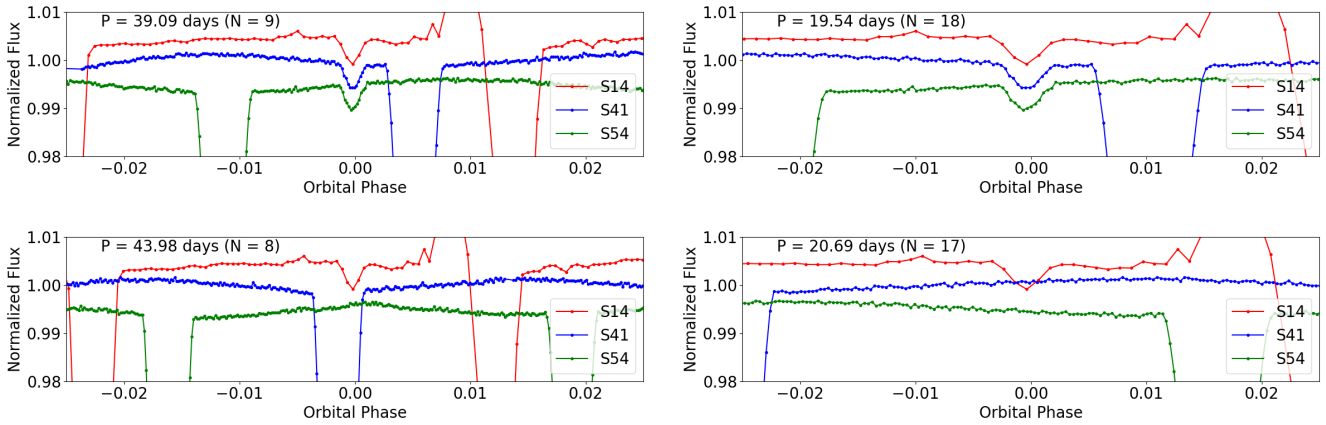

Figure A2. Phase-folded lightcurve for TIC 391461666. Upper panels: fold on two possible periods of the second EB, PB = 351.8/N days: PB = 39.09 days, (i.e., $N = 9$, upper left), and PB = 19.54 days (i.e., $N = 18$, upper right). Both provide a convincing case for binary B and thus a potential true period. Lower panels: same as upper panes, but for two values of N for which PB = 351.8/N days can be ruled out from the available data: $N = 8$ (lower left) and $N = 17$ (lower right).

286779918 in this catalog as a 2+2 eclipsing quadruple candidate.

In an attempt to detect the period of binary B by different means, we observed the target spectroscopically at the Center for Astrophysics with the Tillinghast Reflector Echelle Spectrograph (TRES; A. H. Szentgyorgyi & G. Furész 2007; G. Fürész 2008;) on the 1.5 m Tillinghast reflector, located at the Fred L. Whipple Observatory on Mount Hopkins (Arizona, USA). We gathered 26 spectra covering the wavelength range 3800–9100 Å at a resolving power of $R \approx 44{,}000$, with signal-to-noise ratios of 29–75 per resolution element of 6.8 km s^{-1}. Reductions were carried out with a dedicated pipeline (see L. A. Buchhave et al. 2012). All spectra are double-lined and, as illustrated in Figure A5, both PA components are clearly visible in the radial velocity measurements. The latter were extracted with the two-dimensional cross-correlation algorithm TODCOR (S. Zucker & T. Mazeh 1994). The synthetic templates were taken from a library of calculated spectra based on model atmospheres by Castelli & Kurucz (F. Castelli & R. L. Kurucz 2003) and a line list tuned by hand to improve the match to real stars. We adopted solar metallicity and surface gravities of $\log g = 4.5$ for both PA stars, along with best-fitting effective temperatures of 6250 and 6000 K for the primary and secondary, respectively, and rotational broadenings of 6 km s^{-1} for both stars. The measured velocities and corresponding uncertainties are listed in Table A1. We determined a flux ratio between the components of $\ell_2/\ell_1 = 0.305 \pm 0.005$ at the mean wavelength of our observations (∼5187 Å). A spectroscopic orbital solution gives the elements presented in Table A2, where the symbols have their usual meaning. The orbital period derived from the spectroscopic measurements is $P = 14.29592$ days, fully consistent with the PA = 14.296107 days derived from the TESS photometry for binary A. The rms velocity residuals are 0.14 and 0.34 km s^{-1} for the primary and secondary, and the derived parameters are listed at the bottom of the table. Examination of the spectra with an extension of TODCOR to three dimensions (TRICOR; S. Zucker et al. 1995) revealed no additional stars down to our detection threshold of approximately 1% of the flux of the primary. Thus, our attempt to detect PB spectroscopically failed and the orbital period of binary B remains a mystery at the time of writing.

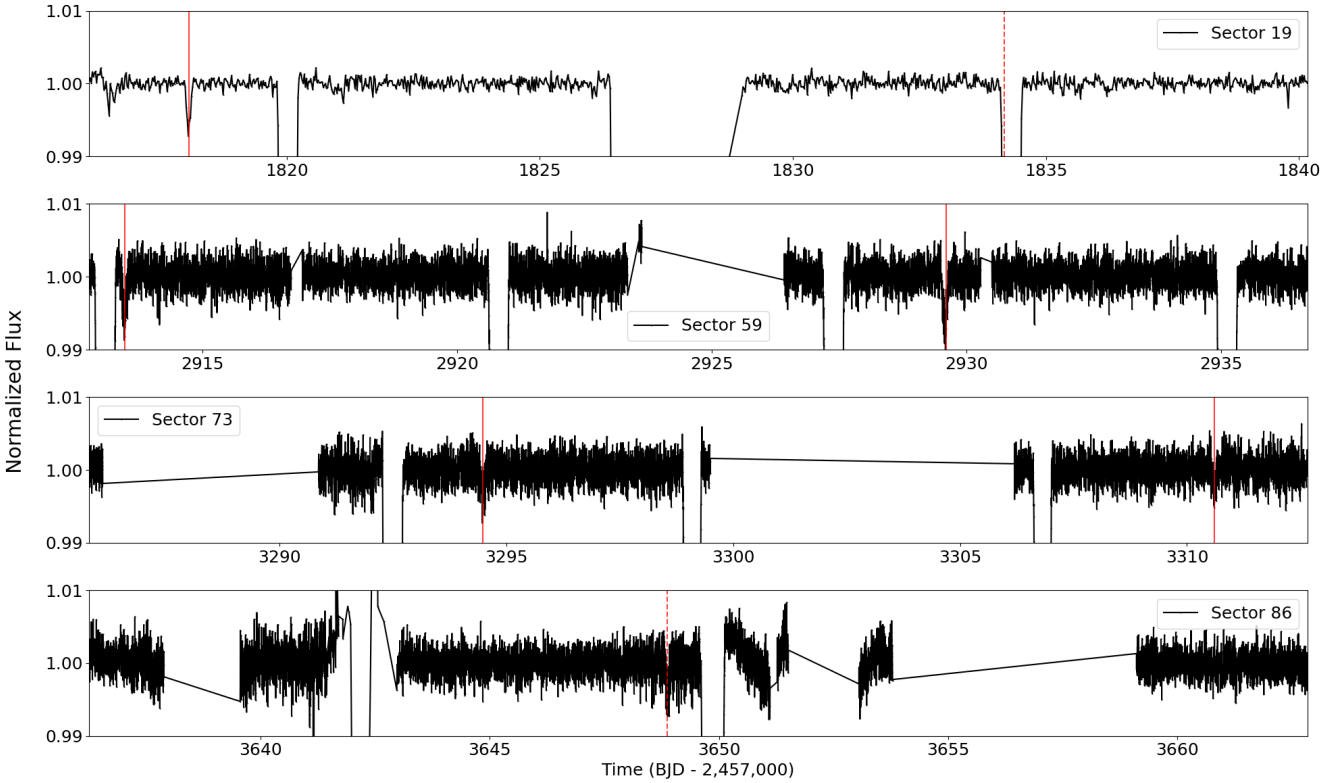

Figure A3. TESS-Gaia lightcurve of TIC 286779918 highlighting the six extra eclipse-like events (vertical red lines).

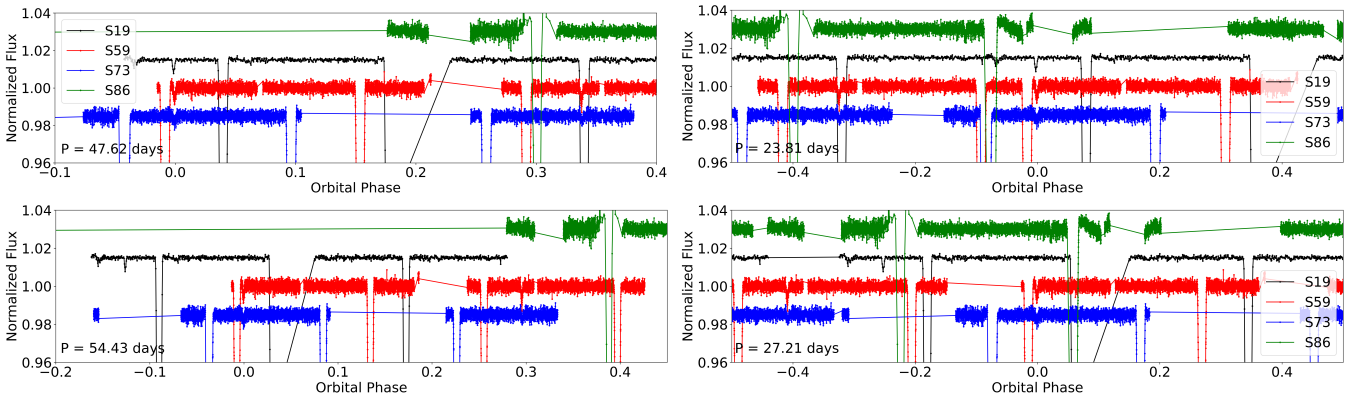

Figure A4. Same as Figure A2 but for TIC 286779918. Upper panels: two test periods that fold three of the extra events: PB $\approx$ 47.6 days (N = 8, upper left) and PB $\approx$ 23.8 days (N = 16, upper right). However, neither period works for all six events. Lower panels: two test periods that fold no more than two of the extra events (centered near zero phase): PB $\approx$ 54.4 days (N = 7, lower left) and PB $\approx$ 27.2 days (N = 14, lower right). Note that the x-axes are different between the different panels, to highlight the phase of potential secondary events.

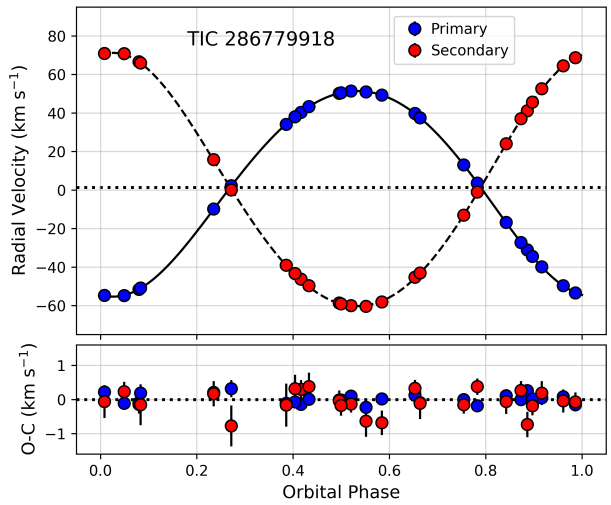

Figure A5. Measured radial velocities and orbit model for TIC 286779918, with residuals shown at the bottom. The dotted line in the top panel represents the center-of-mass velocity.

Table A1
Radial Velocities for TIC 286779918

BJD (2,400,000+)	RV_1 (km s^{-1})	RV_2 (km s^{-1})	σ_1 (km s^{-1})	σ_2 (km s^{-1})
60413.6375	2.29	0.10	0.25	0.60
60417.6382	50.91	−60.32	0.19	0.46
60572.9649	40.35	−46.28	0.11	0.27
60593.9793	−31.09	41.17	0.15	0.37
60604.9379	39.81	−45.24	0.10	0.25
60621.9420	−16.81	24.07	0.15	0.36
60646.8408	49.31	−58.09	0.15	0.36
60653.9306	−51.58	66.57	0.11	0.27
60663.9729	3.61	−0.99	0.10	0.24
60666.8844	−53.35	68.74	0.12	0.28
60677.8653	13.10	−12.99	0.11	0.26
60684.7397	−9.84	15.84	0.15	0.37
60693.8626	−27.21	37.07	0.11	0.27
60710.6766	−54.72	70.78	0.12	0.29
60723.7091	−49.62	64.47	0.14	0.34
60731.7058	51.37	−59.98	0.10	0.25
60738.6836	−54.71	70.89	0.20	0.48
60745.6503	50.24	−58.63	0.13	0.31
60745.7010	50.45	−59.02	0.13	0.30
60751.6612	−39.85	52.63	0.15	0.35
60758.6351	38.07	−43.36	0.17	0.41
60765.6803	−34.48	45.61	0.12	0.28
60772.6682	34.15	−39.06	0.26	0.63
60776.6396	37.46	−43.06	0.19	0.46
60782.6409	−50.82	65.97	0.25	0.60
60787.6392	43.31	−49.65	0.17	0.41

Table A2
Spectroscopic Orbital Parameters for TIC 286779918

Parameter	Value
P (day)	14.29592 ± 0.00033
T_{peri} (BJD)	60667.084 ± 0.0242222
e	0.06367 ± 0.00072
ω_1 (deg)	169.39 ± 0.62
K_1 (km s^{-1})	53.379 ± 0.036
K_2 (km s^{-1})	65.742 ± 0.085
γ (km s^{-1})	+1.370 ± 0.032
Δ_{RV} (km s^{-1})	−0.238 ± 0.079
Derived Properties	
$M_1 \sin^3 i$ ($M_\odot$)	1.3734 ± 0.0039
$M_2 \sin^3 i$ ($M_\odot$)	1.1152 ± 0.0022
$q \equiv M_2/M_1$	0.8119 ± 0.0012
$a \sin i$ ($R_\odot$)	33.594 ± 0.027

Note. The time of periastron passage, T_{peri}, is referred to JD 2,400,000. Parameter Δ_{RV} represents a small velocity zero-point offset between the primary and secondary that is likely due to template mismatch. It was taken into account to avoid biasing the minimum masses. $a \sin i$ is the total projected semimajor axis of the orbit.

Appendix B
Eclipse Timing Measurements

In Table B1 we list the times of eclipse minima for both binaries in quadruple systems that exhibit eclipse timing variations. The full table is available as a machine-readable online supplement.

Table B1
Measured Eclipse Times

TIC	Bin	Time (BJD - 2457000)	Cycle	Std. Dev. (minutes)
48089827	A	1683.7606	−0.5	0.15
48089827	A	1686.1924	0.0	0.08
48089827	A	1688.6233	0.5	0.30
48089827	A	1691.0559	1.0	0.23
...	...	...	...	...
289822938	B	3012.2538	−47.0	0.56[a]
289822938	B	3718.9009	−0.5	0.92[a]
289822938	B	3728.4096	0.0	0.35[a]
289822938	B	3743.6455	1.0	0.44[a]

Note. Table available in full as a machine-readable online supplement.
[a] Stellar variability likely affects the precision of the measurements.

(This table is available in its entirety in machine-readable form in the online article.)

ORCID iDs

V. B. Kostov https://orcid.org/0000-0001-9786-1031
B. P. Powell https://orcid.org/0000-0003-0501-2636
S. A. Rappaport https://orcid.org/0000-0003-3182-5569
T. Borkovits https://orcid.org/0000-0002-8806-496X
R. Gagliano https://orcid.org/0000-0002-5665-1879
T. L. Jacobs https://orcid.org/0000-0003-3988-3245
M. H. Kristiansen https://orcid.org/0000-0002-2607-138X
G. Torres https://orcid.org/0000-0002-5286-0251
G. Handler https://orcid.org/0000-0001-7756-1568
A. R. Schmitt https://orcid.org/0000-0002-5034-0949
H. M. Schwengeler https://orcid.org/0000-0002-1637-2189
D. M. LaCourse https://orcid.org/0000-0002-8527-2114
A. Vanderburg https://orcid.org/0000-0001-7246-5438
S. D. Alexandrov https://orcid.org/0000-0002-4959-8598
C. M. da Silva https://orcid.org/0000-0001-8953-9149
Marco Z. Di Fraia https://orcid.org/0000-0001-7701-6818
Aline U. Fornear https://orcid.org/0000-0001-7062-7632
Julien S. de Lambilly https://orcid.org/0000-0003-3464-1554
R. Rodrigues https://orcid.org/0009-0000-2799-7291
W. Welsh https://orcid.org/0000-0003-2381-5301

References

Abadi, M., Agarwal, A., Barham, P., et al., 2015 TensorFlow: Large-Scale Machine Learning on Heterogeneous Systems, https://www.tensorflow.org/
Ádám, R. Z., Hajdu, T., Bódi, A., et al. 2023, A&A, 674, A170
Andersen, J. 1991, A&ARv, 3, 91
Astropy Collaboration, Price-Whelan, A. M., Lim, P. L., et al. 2022, ApJ, 935, 167
Astropy Collaboration, Price-Whelan, A. M., Sipőcz, B. M., et al. 2018, AJ, 156, 123
Astropy Collaboration, Robitaille, T. P., Tollerud, E. J., et al. 2013, A&A, 558, A33
Belokurov, V., Penoyre, Z., Oh, S., et al. 2020, MNRAS, 496, 1922
Borkovits, T. 2022, Galax, 10, 9
Borkovits, T., Albrecht, S., Rappaport, S., et al. 2018, MNRAS, 478, 5135
Borkovits, T., Derekas, A., Kiss, L. L., et al. 2013, MNRAS, 428, 1656
Borkovits, T., Hajdu, T., Sztakovics, J., et al. 2016, MNRAS, 455, 4136
Borkovits, T., Mitnyan, T., Rappaport, S. A., et al. 2022a, MNRAS, 510 1352
Borkovits, T., Rappaport, S., Hajdu, T., & Sztakovics, J. 2015, MNRAS, 448, 946
Borkovits, T., Rappaport, S. A., Toonen, S., et al. 2022b, MNRAS, 515, 3773
Borkovits, T., Rappaport, S. A., Mitnyan, T., et al. 2025, A&A, 695, A209
Breiter, S., & Vokrouhlický, D. 2018, MNRAS, 475, 5215
Buchhave, L. A., Latham, D. W., Johansen, A., et al. 2012, Natur, 486, 375
Burke, C. J., Levine, A., Fausnaugh, M., et al., 2020 TESS-Point: High Precision TESS Pointing Tool, Astrophysics Source Code Library, ascl: 2003.001
Cacciapuoti, L., Kostov, V. B., Kuchner, M., et al. 2022, MNRAS, 513, 102
Capistrant, B. K., Soares-Furtado, M., Vanderburg, A., et al. 2022, ApJS, 263, 14
Castelli, F., & Kurucz, R. L. 2003, in IAU Symp. 210, Modelling of Stellar Atmospheres, Poster Contributions, ed. N. Piskunov (ASP), A20
Chollet, F., et al. 2015, Keras, https://Keras.io
Czekala, I., Mandel, K. S., Andrews, S. M., et al. 2017, ApJ, 840, 49
Dalcin, L., Paz, R., Storti, M., & D'Elia, J. 2008, JPDC, 68, 655
Deleuil, M., Aigrain, S., Moutou, C., et al. 2018, A&A, 619, A97
Fang, X., Thompson, T. A., & Hirata, C. M. 2018, MNRAS, 476, 4234
Feinstein, A. D., Montet, B. T., Foreman-Mackey, D., et al. 2019, PASP, 131, 094502
Fragione, G., & Kocsis, B. 2019, MNRAS, 486, 4781
Fragos, T., Andrews, J. J., Bavera, S. S., et al. 2023, ApJS, 264, 45
Frieboes-Conde, H., & Herczeg, T. 1973, A&AS, 12, 1
Fürész, G. 2008, PhD thesis, Univ. Szeged
Gaia Collaboration, Brown, A. G. A., Vallenari, A., et al. 2021, A&A, 649, A1
Gandhi, P., Buckley, D. A. H., Charles, P. A., et al. 2022, MNRAS, 510, 3885
Hajdu, T., Borkovits, T., Forgács-Dajka, E., Sztakovics, J., & Bódi, A. 2022, MNRAS, 509, 246
Hamers, A. S., & Lai, D. 2017, MNRAS, 470, 1657
Hamers, A. S., Rantala, A., Neunteufel, P., Preece, H., & Vynatheya, P. 2021, MNRAS, 502, 4479
Han, T., Robertson, P., Brandt, T. D., et al. 2025, ApJL, 988, L4
Handler, G., Kurtz, D. W., Rappaport, S. A., et al. 2020, NatAs, 4, 684
Handler, G., Rappaport, S. A., Jones, D., et al. 2025, A&A, 702, A104
Harris, C. R., Millman, K. J., van der Walt, S. J., et al. 2020, Natur, 585, 357
Hartman, J. D., Bakos, G. Á., Noyes, R. W., et al. 2011, AJ, 141, 166
Heinze, A. N., Tonry, J. L., Denneau, L., et al. 2018, AJ, 156, 241
Huang, C. X., Vanderburg, A., Pál, A., et al. 2020, RNAAS, 4, 204
Hunter, J. D. 2007, CSE, 9, 90
IJspeert, L. W., Tkachenko, A., Johnston, C., et al. 2021, A&A, 652, A120
Jayaraman, R., Rappaport, S. A., Powell, B., et al. 2024, ApJ, 975, 121
Jenkins, M., Twicken, J. D., McCauliff, S., et al. 2016, SPIE, 9913, 99133E
Kochanek, C. S. 2021, MNRAS, 507, 5832
Kochanek, C. S., Shappee, B. J., Stanek, K. Z., et al. 2017, PASP, 129, 104502
Kolář, J., Zejda, M., Richterková, A., et al. 2025, MNRAS, 538, 1160
Kostov, V. B., Borkovits, T., Rappaport, S. A., et al. 2023, MNRAS, 522, 90
Kostov, V. B., Moore, K., Tamayo, D., Jayawardhana, R., & Rinehart, S. A. 2016, ApJ, 832, 183
Kostov, V. B., Powell, B. P., Fornear, A. U., et al. 2025, ApJS, 279, 50
Kostov, V. B., Powell, B. P., Orosz, J. A., et al. 2021a, AJ, 162, 234
Kostov, V. B., Powell, B. P., Rappaport, S. A., et al. 2022, ApJS, 259, 66
Kostov, V. B., Powell, B. P., Rappaport, S. A., et al. 2024, MNRAS, 527, 3995
Kostov, V. B., Powell, B. P., Torres, G., et al. 2021b, ApJ, 917, 93
Kounkel, M., Covey, K. R., Stassun, K. G., et al. 2021, AJ, 162, 184
Kovács, G., Zucker, S., & Mazeh, T. 2002, A&A, 391, 369
Kozai, Y. 1962, AJ, 67, 591
Kristiansen, M. H. K., Rappaport, S. A., Vanderburg, A. M., et al. 2022, PASP, 134, 074401
Lidov, M. L. 1962, P&SS, 9, 719
Lightkurve Collaboration, Cardoso, J. V. d. M., Hedges, C., et al., 2018 Lightkurve: Kepler and TESS Time Series Analysis in Python, Astrophysics Source Code Library, ascl: 1812.013
Liu, B., & Lai, D. 2019, MNRAS, 483, 4060
Lund, M. N., Handberg, R., Buzasi, D. L., et al. 2021, ApJS, 257, 53
Luque, R., Osborn, H. P., Leleu, A., et al. 2023, Natur, 623, 932
Magliano, C., Kostov, V., Cacciapuoti, L., et al. 2023, MNRAS, 521, 3749
Majewski, S., Davidson, J., Wilson, R., et al. 2025, ApJ, 994, 133
Mathieu, R. D. 1994, ARA&A, 32, 465
McKinney, W. 2010, in Proc. 9th Python in Science Conf., ed. S. van der Walt & J. Millman (SciPy), 51
Moe, M., & Di Stefano, R. 2017, ApJS, 230, 15
Mowlavi, N., Holl, B., Lecœur-Taïbi, I., et al. 2023, A&A, 674, 16
Mowlavi, N., Holl, B., Lecoeur-Taïbi, I., et al. 2023, A&A, 674, A16
Orosz, J. A. 2015, ASPC, 496, 55
Pedregosa, F., Varoquaux, G., Gramfort, A., et al. 2011, JMLR, 12, 2825
Pejcha, O., Antognini, J. M., Shappee, B. J., & Thompson, T. A. 2013, MNRAS, 435, 943
Penoyre, Z., Belokurov, V., Wyn Evans, N., Everall, A., & Koposov, S. E. 2020, MNRAS, 495, 321
Pérez, F., & Granger, B. E. 2007, CSE, 9, 21
Pineda, J. E., Offner, S. S. R., Parker, R. J., et al. 2015, Natur, 518, 213
Powell, B. P., Kostov, V. B., Rappaport, S. A., et al. 2021a, AJ, 161, 162
Powell, B. P., Kostov, V. B., Rappaport, S. A., et al. 2021b, AJ, 162, 299
Powell, B. P., Kruse, E., Montet, B. T., et al. 2022, RNAAS, 6, 111
Powell, B. P., Torres, G., Kostov, V. B., et al. 2025, ApJ, 985, 213
Preece, H. P., Hamers, A. S., Battich, T., & Rajamuthukumar, A. S. 2022, MNRAS, 517, 2111
Pribulla, T., Borkovits, T., Jayaraman, R., et al. 2023, MNRAS, 524, 4220
Pribulla, T., Puha, E., Borkovits, T., et al. 2020, MNRAS, 494, 178
Prša, A., Batalha, N., Slawson, R. W., et al. 2011, AJ, 141, 83
Prša, A., Kochoska, A., Conroy, K. E., et al. 2022, ApJS, 258, 16
Raghavan, D., McAlister, H. A., Henry, T. J., et al. 2010, ApJS, 190, 1
Rappaport, S., Vanderburg, A., Borkovits, T., et al. 2017, MNRAS, 467, 2160
Rappaport, S. A., Borkovits, T., Gagliano, R., et al. 2022, MNRAS, 513, 4341
Rappaport, S. A., Borkovits, T., Gagliano, R., et al. 2023, MNRAS, 521, 558
Ricker, G. R., Winn, J. N., Vanderspek, R., et al. 2015, JATIS, 1, 014003
Rowan, D. M., Jayasinghe, T., Stanek, K. Z., et al. 2022, MNRAS, 517, 2190
Rowan, D. M., Jayasinghe, T., Stanek, K. Z., et al. 2023, MNRAS, 523, 2641
Schmitt, A., & Vanderburg, A. 2021, arXiv:2103.10285
Schmitt, A. R., Hartman, J. D., Kipping, D. M., et al. 2019, arXiv:1910.08034
Shara, M. M., Howell, S. B., Furlan, E., et al. 2021, MNRAS, 507, 560

Soszyński, I., Pawlak, M., Pietrukowicz, P., et al. 2016, AcA, 66, 405
Stassun, K. G., & Torres, G. 2021, ApJL, 907, L33
Stassun, K. G., Oelkers, R. J., Paegert, M., et al. 2019, AJ, 158, 138
Stegmann, J., Antonini, F., & Moe, M. 2022, MNRAS, 516, 1406
STScI 2018, TESS Input Catalog and Candidate Target List, STScI/MAST, doi:10.17909/fwdt-2x66
Szentgyorgyi, A. H., & Furész, G. 2007, RMxAC, 28, 129
Tobin, J. J., Kratter, K. M., Persson, M. V., et al. 2016, Natur, 538, 483
Tokovinin, A. 2018, ApJS, 235, 6
Tokovinin, A. 2021, Univ, 7, 352
Torres, G., Andersen, J., & Giménez, A. 2010, A&ARv, 18, 67
Trani, A. A., Rieder, S., Tanikawa, A., et al. 2022, PhRvD, 106, 043014
Tremaine, S. 2020, MNRAS, 493, 5583
Vaessen, T., & van Roestel, J. 2024, A&A, 682, A164
Virtanen, P., Gommers, R., Oliphant, T. E., et al. 2020, NatMe, 17, 261
von Zeipel, H. 1910, AN, 183, 345
Vynatheya, P., & Hamers, A. S. 2022, ApJ, 926, 195
Wang, G., & Espinoza, N. 2024, AJ, 167, 1
Whitworth, A. P. 2001, IAUS, 200, 33
Zasche, P. 2024, A&A, 688, A41
Zasche, P., Henzl, Z., & Kára, J. 2022, A&A, 659, A8
Zasche, P., Henzl, Z., Mašek, M., et al. 2023, A&A, 675, A113
Zasche, P., Henzl, Z., Mašek, M., et al. 2025, MNRAS, 539, 1015
Zasche, P., Vokrouhlický, D., Wolf, M., et al. 2019, A&A, 630, A128
Zucker, S., & Mazeh, T. 1994, ApJ, 420, 806
Zucker, S., Torres, G., & Mazeh, T. 1995, ApJ, 452, 863